Journal of Fluids and Structures (1996) **10,** 565–599

LARGE POST-BUCKLING DEFORMATIONS OF CYLINDRICAL SHELLS CONVEYING VISCOUS FLOW

M. HEIL* AND T. J. PEDLEY
Department of Applied Mathematics, University of Leeds
Leeds, LS2 9JT, U.K.

(Received 14 July 1995 and in revised form 22 April 1996)

This paper examines the post-buckling deformations of cylindrical shells conveying viscous fluid. The wall deformation is modelled using geometrically nonlinear shell theory, and lubrication theory is used to model the fluid flow. The coupled fluid–solid problem is solved using a parallelized FEM technique. It is found that the fluid–solid interaction leads to a violent collapse of the tube such that immediate opposite-wall contact occurs after the buckling if the volume flux is kept constant during buckling. If the pressure drop through the tube is kept constant during the buckling, the fluid–solid coupling slows down the collapse (compared to buckling under a dead load). The effects of various parameters (upstream pressure, axial pre-stretch and the geometry of the tube) on the post-buckling behaviour are examined and the exact geometrically nonlinear shell theory is compared to Sanders' (1963) moderate rotation theory. Finally, the implications of the results for previous models which described the wall deformation using so called ''tube laws'' are discussed.

1. INTRODUCTION

THE PROBLEM OF FLOW THROUGH COLLAPSIBLE tubes has been studied both theoretically and experimentally by many authors [for a review see Kamm & Pedley (1989)]. The main motivation for this work comes from the investigation of certain biological flows such as blood flow in veins and arteries or air flow in the bronchial airways during forced expiration. The tubes collapse when the transmural pressure difference (internal minus external pressure) falls below a critical level. Following the collapse, self-excited oscillations can be observed for a wide range of parameters.

A typical experimental setup is shown in Figure 1. Inside a pressure chamber, a finite-length collapsible tube is mounted on two rigid tubes, and viscous fluid is pumped through. Various combinations of parameters can be varied in the experiments (e.g. external pressure and volume flux or external pressure and upstream pressure, etc.). For sufficiently large external pressure and/or volume flux, the tube collapses at the downstream end, i.e. it buckles nonaxisymmetrically [see, e.g., Elad *et al.* (1992)].

So far, most theoretical models of the complex interaction between fluid and solid mechanics have used relatively simple ''tube laws'' to describe the elastic behaviour of the tube wall. These tube laws relate the cross-sectional area of the tube to the local transmural pressure difference. The fluid flow was either modelled one-dimensionally or *ad hoc* assumptions about the shape of the deformed cross-sectional area had to be

* Present address: Room 3-260, Department of Mechanical Engineering, Massachusetts Institute of Technology, Cambridge, MA 02139, U.S.A.

0889–9746/96/060565 + 35 $18.00

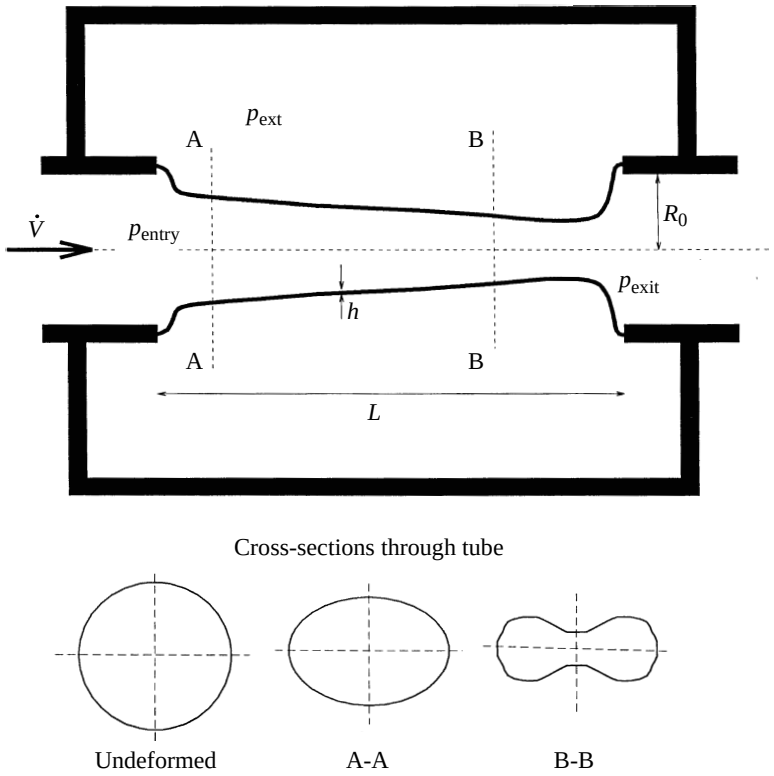

Figure 1. Sketch of the model problem.

made (Wild *et al.* 1977). Membrane theory has been used to model axisymmetric deformations of the tube [e.g. Hart & Shi (1992) who modelled the axisymmetric deformation of semi-infinite tubes composed of sections of different materials] but these models cannot be used to investigate the post-buckling behaviour of the collapsed tube. Heil & Pedley (1995) studied the large axisymmetric deformations of finite-length collapsible tubes using geometrically nonlinear shell theory for the tube wall and lubrication theory for the fluid flow. The mechanisms involved in the pre-buckling deformation were examined for boundary conditions corresponding to a variety of experimental setups.

Heil (1995a) investigated the linear stability of this system to establish the critical parameter combinations (upstream pressure and volume flux) for which the axisymmetric deformation of the tube becomes unstable. The most unstable wavenumbers and the corresponding linear buckling modes were determined for tubes of various geometries.

In this paper, we extend the axisymmetric model developed by Heil & Pedley (1995) to the non-axisymmetric post-buckling deformations of the tube. The outline of the paper is as follows: in Section 2.1 we present a brief summary of the shell theory used to describe the large deformations of the tube wall. The fluid model is derived in Section 2.2 and Section 2.3 explains the coupling between fluid and solid mechanics. Details of the numerical solution of the coupled problem are given in Section 3. The results of our computations are presented and discussed in Section 4. We investigate the post-buckling behaviour of the tube with and without fluid-solid coupling and examine the effect of changes in various parameters (upstream pressure, axial

pre-stretch and changes in the tube geometry) on the post-buckling. The exact geometrically nonlinear shell theory is compared to Sanders' (1963) moderate rotation theory. Finally, we discuss the implications of our results for models which were based on the simpler ''tube laws''.

2. THE MODEL

2.1. Shell Theory

We model the tube of length, L, undeformed radius, R_0, and wall thickness, h, as a cylindrical shell and describe its deformation using a geometrically nonlinear Kirchhoff-Love type shell theory [e.g., Wempner (1973)]. Using the usual assumptions (thickness of the shell is constant, normals to the undeformed midplane remain normal), the deformation of the shell can be expressed in terms of the midplane displacements $\tilde{\mathbf{v}}$. We use Lagrangian coordinates $\tilde{x}^\alpha$ (Greek and Latin indices have values $1, 2$ and $1, 2, 3$, respectively, and the summation convention is used) to parameterize the shell mid-plane. Let $\tilde{\boldsymbol{r}}^0(\tilde{x}^\alpha)$ be the vector to a material point on the mid-plane before deformation. We choose cylindrical coordinates as the Lagrangian coordinates ($\tilde{x}^1$ and $\tilde{x}^2$ are the arclengths in the axial and circumferential direction, respectively). Lower case letters refer to the undeformed reference state, the tilde denotes dimensional quantities and the superscript ''0'' indicates the vector to the midplane:

$$\tilde{\boldsymbol{r}}^0 = (R_0 \sin(\tilde{x}^2/R_0),\, R_0 \cos(\tilde{x}^2/R_0),\, \tilde{x}^1)^{\mathrm{T}}, \quad \tilde{x}^1 \in [0,\, L], \quad \tilde{x}^2 \in [0,\, 2\pi R_0]. \tag{1}$$

The position of an arbitrary point in the shell at a distance $\tilde{x}^3$ from the mid-plane can be written as (see Figure 2):

$$\tilde{\boldsymbol{r}} = \tilde{\boldsymbol{r}}^0 + \tilde{x}^3 \boldsymbol{n}, \qquad \tilde{x}^3 \in [-h/2,\, h/2]; \tag{2}$$

$\boldsymbol{n} = \boldsymbol{a}_3$ is the unit vector normal to the two midplane base vectors $\boldsymbol{a}_\alpha = \tilde{\boldsymbol{r}}^0_{,\alpha}$ where the comma denotes partial differentiation with respect to $\tilde{x}^\alpha$. Let $\alpha_{\alpha\beta} = \boldsymbol{a}_\alpha \cdot \mathbf{a}_\beta$ be the

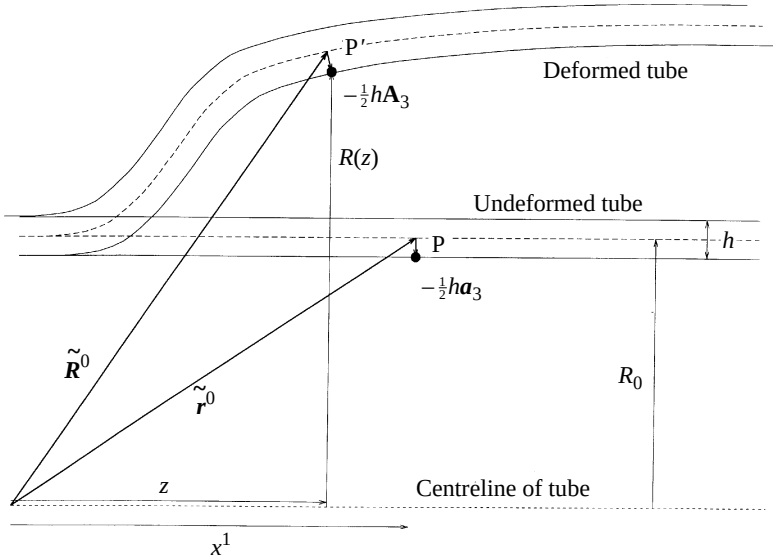

Figure 2. Transformation between the Lagrangian coordinates used for the description of the tube wall and the Eulerian fluid coordinates: the material point P on the inner surface of the undeformed tube wall is moved to P′. Note that for nonaxisymmetric deformations the vectors do not necessarily lie in the same plane.

covariant midplane metric tensor, a its determinant and $\tilde{b}_{\alpha\beta} = \boldsymbol{n} \cdot \boldsymbol{a}_{\alpha,\beta}$ the curvature tensor of the undeformed midplane. After the deformation, the material point on the midplane with the Lagrangian coordinates $\tilde{x}^\alpha$ has been displaced to a new position $\tilde{\boldsymbol{R}}^0(\tilde{x}^\alpha) = \tilde{\boldsymbol{r}}^0(\tilde{x}^\alpha) + \tilde{\boldsymbol{v}}(\tilde{x}^\alpha)$. We decompose the displacement vector, $\tilde{\boldsymbol{v}}$, into the undeformed basis, $\tilde{\boldsymbol{v}} = \tilde{v}^j \boldsymbol{a}_j$. We use capital letters for the quantities associated with the deformed tube: midplane base vectors $\boldsymbol{A}_\alpha = \tilde{\boldsymbol{R}}^0_{,\alpha}$, unit normal $\boldsymbol{N} = \boldsymbol{A}_3$, midplane metric tensor $A_{\alpha\beta} = \boldsymbol{A}_\alpha \cdot \boldsymbol{A}_\beta$, curvature tensor $\tilde{B}_{\alpha\beta} = \boldsymbol{N} \cdot \boldsymbol{A}_{\alpha,\beta}$ and vector to a point in the deformed shell

$$\tilde{\boldsymbol{R}} = \tilde{\boldsymbol{R}}^0 + \tilde{x}^3 \boldsymbol{N}. \tag{3}$$

Then the deformation is described by the strain tensor $\gamma_{\alpha\beta} = \frac{1}{2}(A_{\alpha\beta} - a_{\alpha\beta})$ and the bending tensor $\tilde{\kappa}_{\alpha\beta} = -(\tilde{B}_{\alpha\beta} - \tilde{b}_{\alpha\beta})$. In spite of the large deformations, the strain of the shell is still relatively small [Elad *et al.* (1992) report about 2–3% maximum extension in their experiments]; therefore, we use Hooke's law (linear constitutive equations) and Love's first approximation to express the strain energy function, $\tilde{\phi}$ (strain energy per unit area of the undeformed mid-plane of the shell) in terms of the strain and bending tensors:

$$\tilde{\phi} = \tfrac{1}{2} h \tilde{E}^{\alpha\beta\gamma\delta} (\gamma_{\alpha\beta}\gamma_{\gamma\delta} + \tfrac{1}{12} h^2 \tilde{\kappa}_{\alpha\beta}\tilde{\kappa}_{\gamma\delta}), \tag{4}$$

with the plane stress stiffness tensor

$$\tilde{E}^{\alpha\beta\gamma\delta} = \frac{E}{2(1+\nu)} \left(a^{\alpha\gamma}a^{\beta\delta} + a^{\alpha\delta}a^{\beta\gamma} + \frac{2\nu}{1-\nu} a^{\alpha\beta}a^{\gamma\delta} \right), \tag{5}$$

where E is Young's modulus, ν is Poisson's ratio and $a^{\alpha\beta}$ is the contravariant metric tensor of the undeformed midplane, $a^{\alpha\beta}a_{\beta\gamma} = \delta^\alpha_\gamma$. (It should be noted that the strain in actual physiological conduits can be quite large and that Hooke's law cannot be expected to yield an accurate description of their stress-strain behaviour.)

We use the principle of virtual displacements

$$\int_0^{2\pi R_0} \int_0^L (\delta\tilde{\phi} - (\tilde{\boldsymbol{f}} \cdot \delta\tilde{\boldsymbol{R}})|_{\tilde{x}^3 = \pm h/2}) \sqrt{a}\, \mathrm{d}\tilde{x}^1\, \mathrm{d}\tilde{x}^2 = 0, \tag{6}$$

where $\tilde{\boldsymbol{f}}$ is the load per unit area of the undeformed midplane. Since the loads act on the outer surfaces of the shell, we decompose them into the base vectors $\boldsymbol{G}_i = \tilde{\boldsymbol{R}}_{,i}$ on these surfaces (due to the finite thickness of the shell, the $\boldsymbol{G}_i$ can differ from the midplane base vectors $\boldsymbol{A}_i$). Using (3) we obtain the base vectors at a distance $\tilde{x}^3$ from the midplane,

$$\tilde{\boldsymbol{G}}_\alpha = \boldsymbol{A}_\alpha - \tilde{x}^3 \tilde{B}^{\cdot\beta}_{\alpha} \boldsymbol{A}_\beta \quad \text{and} \quad \boldsymbol{G}_3 = \boldsymbol{A}_3. \tag{7}$$

The deformed mixed variance curvature tensor is given by

$$\tilde{B}^{\cdot\beta}_{\alpha} = \tilde{B}_{\alpha\gamma} A^{\gamma\beta}, \tag{8}$$

where $A^{\gamma\beta}$ is the contravariant metric tensor of the deformed midplane, $A_{\alpha\gamma}A^{\gamma\beta} = \delta^\beta_\alpha$. The corresponding components of the metric tensor are $G_{\alpha\beta} = \boldsymbol{G}_\alpha \cdot \boldsymbol{G}_\beta$, $G_{33} = 1$ and $G_{3\alpha} = 0$. Area elements on the surface $\tilde{x}^3 = \text{const.}$ are given by $\mathrm{d}\mathscr{A} = \sqrt{G}\, \mathrm{d}\tilde{x}^1\, \mathrm{d}\tilde{x}^2$, where G is the determinant of the metric tensor $G_{\alpha\beta}$. We express the load terms in (6) in terms of the physical loads, $\tilde{\tau}^i$, as

$$\tilde{\boldsymbol{f}} \sqrt{a}\, \mathrm{d}\tilde{x}^1\, \mathrm{d}\tilde{x}^2 = \left(\tilde{\tau}^\alpha \frac{\boldsymbol{G}_\alpha}{\sqrt{G_{(\alpha\alpha)}}} + \tilde{\tau}^3 \boldsymbol{G}_3 \right) \sqrt{G}\, \mathrm{d}\tilde{x}^1\, \mathrm{d}\tilde{x}^2. \tag{9}$$

It should be noted that the deformed tangential base vectors, $\boldsymbol{G}_\alpha$ (which we normalized by their lengths $\sqrt{G_{(\alpha\alpha)}}$ are not necessarily orthogonal.

We nondimensionalize the coordinates $\tilde{x}^i$, the displacements $\tilde{\boldsymbol{v}}$ and the bending tensor, $\tilde{\kappa}_{\alpha\beta}$ with the undeformed radius, $\tilde{x}^i = x^i R_0$, $\tilde{\boldsymbol{v}} = \boldsymbol{v} R_0$, $\tilde{\kappa}_{\alpha\beta} = \kappa_{\alpha\beta}/R_0$ and the stiffness tensor and the loads with Young's modulus, $\tilde{E}^{\alpha\beta\gamma\delta} = E^{\alpha\beta\gamma\delta}E$ and $\tilde{\boldsymbol{f}} = \boldsymbol{f}E$. The strain tensor, $\gamma_{\alpha\beta}$, is already dimensionless. Then we obtain the following variational equation for the equilibrium of the tube wall

$$\int_0^{2\pi}\int_0^{L/R_0}\left[E^{\alpha\beta\gamma\delta}\left(\gamma_{\alpha\beta}\delta\gamma_{\gamma\delta} + \frac{1}{12}\left(\frac{h}{R_0}\right)^2\kappa_{\alpha\beta}\delta\kappa_{\gamma\delta}\right) - \left(\frac{R_0}{h}\right)(\boldsymbol{f}\cdot\delta\boldsymbol{R})|_{x^3=\pm h/(2R_0)}\right]\sqrt{a}\,\mathrm{d}x^1\,\mathrm{d}x^2 = 0, \quad (10)$$

where the variations of strain and bending tensor have to be taken with respect to the displacements v^i and their derivatives. The tube is clamped at both ends. Therefore, at $x^1 = 0$ and $x^1 = L/R_0$ the displacements have to be prescribed (which allows the possibility of pre-stretch) and we have $\mathrm{d}v^3/\mathrm{d}x^1 = 0$. This formulation is valid for arbitrary deformations as long as the strains are small enough to justify the use of Hooke's law. This small strain assumption implies that the large deformations of the tube correspond to large rigid body rotations. Therefore, we used the exact, fully nonlinear expressions for the strain and bending tensors and did not introduce any further simplifications in the strain displacement relations. Sanders (1963) developed a shell theory for small strains and moderately large rotations which has been widely used for similar problems. In Section 4 we will examine the validity of his simplified theory for the present problem.

2.2. Fluid Mechanics

For physiologically realistic values of the Reynolds number (Pedley 1980), the fluid mechanics would be governed by the full Navier-Stokes equations. However, the numerical solution of the full Navier–Stokes equations coupled to the highly nonlinear shell equations, described above, would be so computationally expensive that even today's most powerful computers would still be too slow. It is therefore essential to simplify either the shell theory or the fluid mechanics to make any progress. Since the main emphasis of this work is on the development of an improved model for the wall deformation, we assume, for simplicity, that the wall slope in the streamwise direction (α, say) and its product with the Reynolds number are small everywhere. This allows us to simplify the equations considerably. The validity of this assumption will be discussed in Section 4.

We use Eulerian cylindrical polar coordinates $(\tilde{r}, \tilde{z}, \varphi) = (rR_0, zR_0, \varphi)$ for the fluid flow and base the Reynolds number on the average axial fluid velocity $\bar{U}$, i.e. $\mathrm{Re} = \bar{U}R_0/\nu$, where ν is the kinematic viscosity of the fluid. Under the assumption $\alpha \ll 1$, the equation of continuity provides a scaling for the velocity components, $\tilde{u}_r/\tilde{u}_z$, $\tilde{u}_\varphi/\tilde{u}_z = \mathcal{O}(\alpha) \ll 1$. The use of this scaling and the assumption $\mathrm{Re}\,\alpha \ll 1$ in the momentum equation shows that, at leading order, the fluid pressure, $\tilde{p}$, is only a function of the axial coordinate $\tilde{z}$, i.e. $\tilde{p} = \tilde{p}(\tilde{z})$.

We scale the z-component of the velocity as $\tilde{u}_z = u_z\dot{V}/R_0^2$, where $\dot{V}$ is the volume flux through the tube, and nondimensionalize the pressure with Young's modulus, $\tilde{p} = pE$. Then the z-component of the momentum equation is given by

$$\frac{\partial p}{\partial z} = q\,\frac{\pi R_0}{8L}\nabla^2 u_z, \quad (11)$$

where ∇^2 stands for the nondimensional Laplace operator in the $(r-\varphi)$-plane. The parameter q represents the nondimensional pressure drop through an undeformed tube of length L and inner radius R_0,

$$q = \frac{8\mu \dot{V} L}{\pi R_0^4 E}. \tag{12}$$

Since q is proportional to $\dot{V}$ we will regard it as the nondimensional volume flux. The parabolic equation (11) is subject to the normalization condition

$$\int_{A(z)} u_z \, \mathrm{d}A = 1, \tag{13}$$

which requires that the same volume flux, $\dot{V}$, passes through every cross-section $A(z)$, and to a no-slip boundary condition on the tube walls ∂A,

$$u_z\big|_{\partial A} = 0. \tag{14}$$

At one z-coordinate, an initial value for the pressure has to be prescribed, e.g. $p\big|_{z=0} = p_{\text{entry}}$. Physically, these equations imply that the flow through every cross-section $A(z)$ is identical to the flow through an infinitely long tube of the same (constant) cross-section [see also Ribreau *et al.* (1994)].

The fluid stress vector, $\boldsymbol{t}$, at the tube wall is obtained from the stress tensor $\underline{\boldsymbol{T}}$ and the normal vector $\boldsymbol{N}$,

$$\boldsymbol{t} = \underline{\boldsymbol{T}} \cdot \boldsymbol{N}, \tag{15}$$

where the normal vector $\boldsymbol{N}$ is the third base vector on the shell surface, $\boldsymbol{N} = \boldsymbol{G}_3 = \boldsymbol{A}_3$. In the Eulerian cylindrical polar coordinates, we write this vector as

$$\boldsymbol{N} = N_r \boldsymbol{e}_r + N_z \boldsymbol{e}_z + N_\varphi \boldsymbol{e}_\varphi, \tag{16}$$

where the $\boldsymbol{e}_r$, $\boldsymbol{e}_z$, $\boldsymbol{e}_\varphi$ are unit vectors in radial, axial and circumferential direction, respectively (see Figure 3). The components of N are

$$N_r = \cos\beta \cos\gamma, \quad N_z = \sin\beta, \quad N_\varphi = \cos\beta \sin\gamma. \tag{17, 18, 19}$$

Figure 3 shows that β is the angle at which the normal vector $\boldsymbol{N}$ is inclined to the $(r\text{-}\varphi)$-plane. Our assumption about the small wall slope in the axial direction implies that $\beta = \mathcal{O}(\alpha) \ll 1$. γ is the angle between the projection of the normal vector $\boldsymbol{N}$ onto the $(r\text{-}\varphi)$-plane and the radial unit vector $\boldsymbol{e}_r$.

Inserting the velocity scalings, derived above, into the stress tensor $\underline{\boldsymbol{T}}$ for a Newtonian fluid in cylindrical polar coordinates and nondimensionalizing all stresses with Young's modulus E, we obtain the following approximation for the stress vector:

$$\boldsymbol{t} = t_r \boldsymbol{e}_r + t_z \boldsymbol{e}_z + t_\varphi \boldsymbol{e}_\varphi, \tag{20}$$

with

$$t_r = -p \cos\beta \cos\gamma, \quad t_z = -p \sin\beta + \tau_w \cos\beta, \quad t_\varphi = -p \cos\beta \sin\gamma. \tag{21, 22, 23}$$

In these equations we could set $\cos\beta = 1$ without any further loss of accuracy but we keep the "exact" expressions to ensure that the pressure acts normal to the tube wall even for larger wall slopes.

The nondimensional wall shear stress, τ_w, is given by

$$\tau_w = q \frac{\pi R_0}{8L} \frac{\partial u_z}{\partial n}, \tag{24}$$

where $\partial/\partial n$ stands for the normal derivative in the $(r\text{-}\varphi)$-plane.

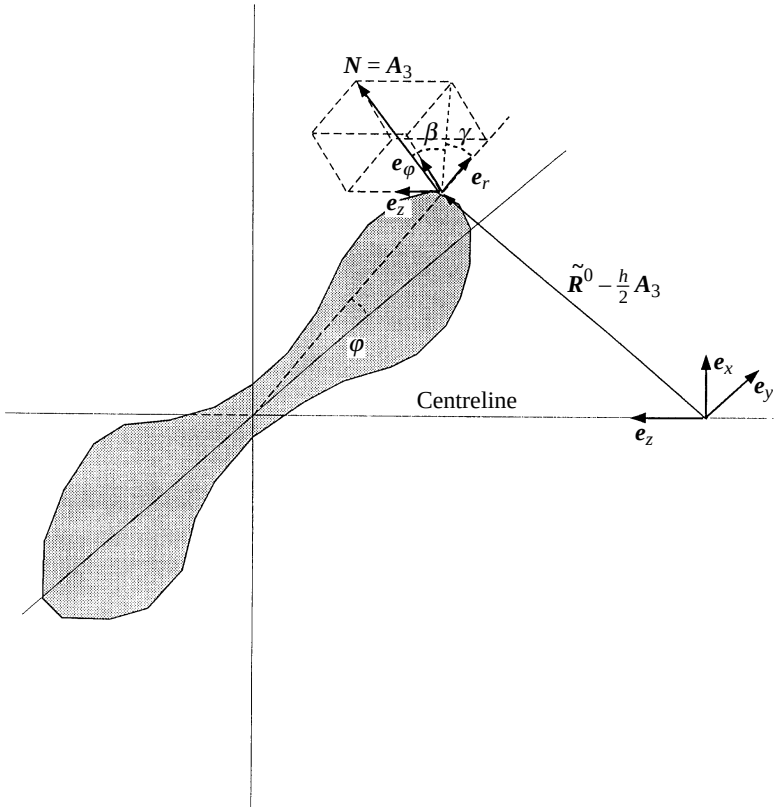

Figure 3. Sketch of the decomposition of the normal vector $\boldsymbol{N}$. The vector $\tilde{\boldsymbol{R}}^0 - h/2\mathbf{A}_3$ leads to a point on the inside of the tube wall, where the normal vector $\boldsymbol{N}$ has to be decomposed into the Eulerian cylindrical polar coordinates. The tube cross-section, in the (r-φ)-plane, is shaded. β is the angle at which the normal vector $\boldsymbol{N}$ is inclined to the (r-φ)-plane and γ is the angle between the projection of $\boldsymbol{N}$ onto the (r-φ)-plane and the radial unit vector $\boldsymbol{e}_r$.

2.3. Fluid-Solid Coupling

Fluid and solid mechanics are coupled through the wall position and through the traction exerted by the fluid on the tube wall. Since two different coordinate systems have been used for fluid and solid mechanics, the stress vector and displacements have to be transformed from one coordinate system to the other.

By following the path of a particle with Lagrangian coordinates (x^1, x^2) on the inner tube wall during the deformation (Figure 2) we obtain its axial coordinate

$$z(x^1, x^2) = \left(\boldsymbol{R}^0 - \frac{h}{2R_0}\boldsymbol{A}_3\right) \cdot \boldsymbol{a}_1, \tag{25}$$

and its radial position

$$R_{\text{tube}}(x^1, x^2) = \sqrt{\left|\boldsymbol{R}^0 - \frac{h}{2R_0}\boldsymbol{A}_3\right|^2 - z^2}\,. \tag{26}$$

This transformation is valid for arbitrary deformations but for nonaxisymmetric deformations the vectors in Figure 2 do not necessarily lie in the same plane. Figure 3 shows that the Eulerian polar angle, φ, of a particle on the tube wall is obtained from

$$\tan\varphi(x^1, x^2) = \frac{[\boldsymbol{R}^0 - (h/2R_0)\boldsymbol{A}_3] \cdot \boldsymbol{e}_x}{[\boldsymbol{R}^0 - (h/2R_0)\boldsymbol{A}_3] \cdot \boldsymbol{e}_y}. \tag{27}$$

The angles β and γ are given by

$$\sin\beta = \boldsymbol{A}_3 \cdot \boldsymbol{a}_1 \tag{28}$$

and

$$\sin\gamma = \frac{\boldsymbol{A}_3 \cdot \boldsymbol{e}_x \cos\varphi - \boldsymbol{A}_3 \cdot \boldsymbol{e}_y \sin\varphi}{\cos\beta}. \tag{29}$$

Given the displacement field $v^i(x^1, x^2)$, all quantities on the right-hand side of the above equations are determined. Hence, these equations are the transformation between the Lagrangian coordinates used for the solid mechanics and the Eulerian coordinates of the inner surface of the tube, as needed for the solution of the fluid equations.

The traction exerted by the fluid on the wall is opposite to the traction exerted by the wall on the fluid. Hence, the fluid stress vector $\boldsymbol{t}$ and the load components τ^i, used in the shell equations, are related by

$$\boldsymbol{t} = t_r \boldsymbol{e}_r + t_z \boldsymbol{e}_z + t_\varphi \boldsymbol{e}_\varphi = -\left(\tau^\alpha \frac{\boldsymbol{G}_\alpha}{\sqrt{G_{(\alpha\alpha)}}} + \tau^3 \boldsymbol{G}_3 \right). \tag{30}$$

This is a system of three linear equations which can be solved for the load components τ^i.

Obviously, the model is not entirely self-consistent: the fluid traction has been derived under the assumption of a small wall slope whereas the shell theory and the transformation of the fluid traction to the shell coordinates are both valid for arbitrarily large rotations of material lines. Since we did not use the small slope assumption in the transformation of the fluid traction, any future improvement of the model can be restricted to the fluid mechanics.

3. NUMERICAL IMPLEMENTATION

Since the wall deformation changes the geometry of the fluid domain, fluid and solid mechanics are strongly coupled and both problems need to be solved simultaneously. Before giving details of the numerical solution, we outline the general solution strategy.

In Section 3.1 we will discretize the shell equations using a FEM technique and thereby transform the variational equation (10) into a system of N_{FEM} nonlinear algebraic equations for the discretized displacements $\mathcal{V}_i$ ($i = 1, N_{\mathrm{FEM}}$). The discretized shell equations also depend on the fluid traction $\boldsymbol{f}$, therefore they have the form $\mathcal{S}_j(\mathcal{V}_i, \boldsymbol{f}) = 0$ ($i,j = 1, N_{\mathrm{FEM}}$).

In Section 3.2 we shall solve the fluid equations and determine the fluid traction $\boldsymbol{f}$ for a given deformation of the tube. Thus, we shall obtain the fluid traction as a function of the discretized displacements, i.e. $\boldsymbol{f} = \boldsymbol{f}(\mathcal{V}_i)$. This allows us to write the discretized shell equations as

$$\mathcal{S}_j(\mathcal{V}_i, \boldsymbol{f}(\mathcal{V}_i)) = 0, \quad i, j = 1, N_{\mathrm{FEM}}. \tag{31}$$

We shall solve this system of equations using the Newton-Raphson method and determine the elements of the Jacobian matrix by finite differencing with respect to the discretized displacement variables. While this procedure is essentially based on the shell equations, the fluid flow is fully incorporated. The use of this strategy avoids the "switching" between fluid and solid solver that has been used by other authors [e.g., Lowe & Pedley (1995)] and guarantees the quadratic convergence rate of the Newton-Raphson method.

TABLE 1
Table of the local coordinates of the four nodes in each shell element

j	s_1	s_2
1	0	0
2	1	0
3	1	1
4	0	1

3.1. NUMERICAL SOLUTION OF THE SHELL EQUATIONS

Since a variational equation exists for the solid mechanics, a displacement-based finite element technique was chosen to discretize the equations. Carrying out the variations in (10) is a straightforward process but involves some lengthy algebra. We used the symbolic formula manipulator REDUCE to express (10) in terms of the displacements and their derivatives. Equation (10) can thereby be written as

$$\int_0^{2\pi}\int_0^{L/R_0} (\phi_i \delta v^i + \phi_{i\alpha}\delta v^i_{,\alpha} + \phi_{i\alpha\beta}\delta v^i_{,\alpha\beta})\sqrt{a}\,\mathrm{d}x^1\,\mathrm{d}x^2 = 0. \tag{32}$$

The ϕ terms contain up to second derivatives of the displacements; therefore, we need shape functions with continuous first derivatives across the element boundaries. We used quadrilateral isoparametric Hermite elements with nodal displacements and slopes as independent degrees of freedom (Bogner *et al.* 1967). Within the element number E the displacements, v^i, were interpolated as

$$v^i = \sum_{j,k=1}^{4} V^{iJ(j,E)k}\psi_{jk}(s_1, s_2). \tag{33}$$

The shape functions were chosen to be tensor products of the one-dimensional Hermite polynomials $h_1(s) = 2s^3 - 3s^2 + 1$, $h_2(s) = s^3 - 2s^2 + s$, $h_3(s) = -(2s^3 - 3s^2)$ and $h_4(s) = s^3 - s^2$. The first index of the shape function ψ_{jk} stands for the local node number ($j = 1,4$). Table 1 shows the local coordinates of the four nodes in each shell element. The second index ($k = 1,4$) of the shape function stands for the type of the degree of freedom, such that at local node j the shape function, ψ_{jk}, fulfils the relations given in Table 2. For instance, the shape function interpolating the s_1-derivative at node 3 is $\psi_{32}(s_1, s_2) = h_4(s_1)h_3(s_2)$. $J(j, E)$ is the global node number corresponding to the local

TABLE 2
Value of the shape functions ψ_{jk} at node j in each element

k	ψ_{jk}	$\partial\psi_{jk}/\partial s_1$	$\partial\psi_{jk}/\partial s_2$	$\partial^2\psi_{jk}/\partial s_1\,\partial s_2$	ψ_{jk} interpolates
1	1	0	0	0	the displacement
2	0	1	0	0	the s_1-derivative
3	0	0	1	0	the s_2-derivative
4	0	0	0	1	the mixed derivative

node number j ($j = 1,4$) in element number E. To generate isoparametric elements, we used the same shape functions to map the local coordinates (s_1, s_2) to the global coordinates (x^1, x^2),

$$x^\alpha = \sum_{j,k=1}^{4} X^{\alpha J(j,E)k} \psi_{jk}(s_1, s_2). \tag{34}$$

This mapping has to interpolate the x^α-coordinates of the nodal points J, x^α_J, therefore we have $X^{\alpha J1} = x^\alpha_J$. The derivatives of the mapping can have any positive value but the mapping has to fulfil the following two conditions: (i) its derivatives have to be continuous across the element boundaries; (ii) it has to be one-to-one everywhere.

We only use rectangular meshes with variable mesh spacing; therefore, the nodal points lie on lines $x^\alpha = \text{const}$. Due to the properties of the Hermite base functions, the derivative of the mapping function at the nodal point J with respect to the local coordinates is

$$\left.\frac{\partial x^\alpha}{\partial s_1}\right|_J = X^{\alpha J2} \quad \text{and} \quad \left.\frac{\partial x^\alpha}{\partial s_2}\right|_J = X^{\alpha J3}. \tag{35}$$

It can be shown that the mapping in (34) fulfils conditions (i) and (ii) if we choose the coefficients $X^{\alpha J2}$ and $X^{\alpha J3}$ to be equal to the minimum size of the elements sharing node J, i.e.

$$X^{1J2} = \text{Min}(\Delta_{4J}, \Delta_{J2}) \quad \text{and} \quad X^{2J3} = \text{Min}(\Delta_{1J}, \Delta_{J3}). \tag{36}$$

Δ_{4J} and Δ_{J2} are the widths of the elements sharing node J, and Δ_{1J} and Δ_{J3} are their heights; see Figure 4. For nodes which lie on the boundary of the domain, the coefficients were chosen to be equal to the size of the adjacent elements inside the domain. For a rectangular mesh, all other coefficients $X^{\alpha Jk}$ can be set to zero.

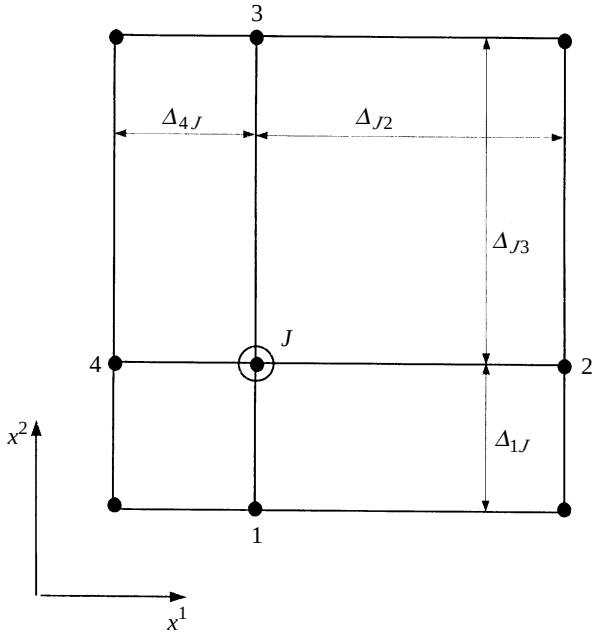

Figure 4. Sketch illustrating the isoparametric mapping used to generate isoparametric Hermite elements. On a rectangular mesh, each interior node J is shared by four elements. Their widths and heights, Δ, in the x^1 and x^2 directions are used to assign the values of the derivatives of the isoparametric mapping at node J.

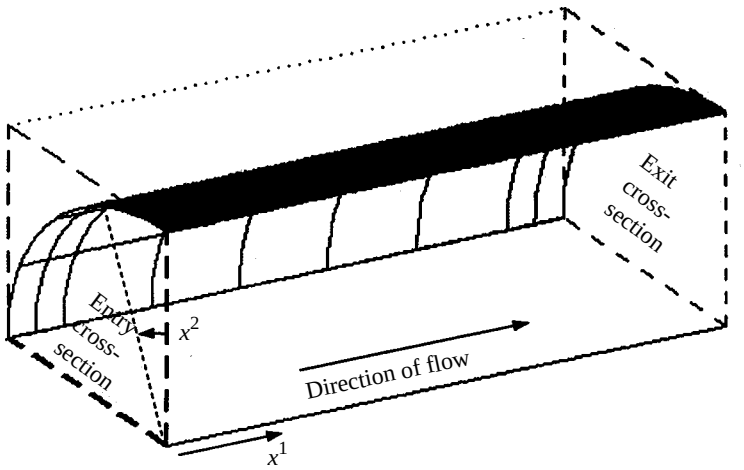

Figure 5. Sketch of the undeformed tube and its FEM discretization. Due to the symmetry of the deformation, only one quarter of the tube needs to be discretized for a circumferential buckling wavenumber of $N_{\text{buckl}} = 2$.

The buckled configuration of the tube is symmetric, and hence we only discretize one quarter of the tube (see Figure 5) for buckling modes with $N_{\text{buckl}} = 2$ waves in the circumferential direction, and an appropriately smaller fraction for higher buckling wavenumbers. The tube is clamped at the upstream and downstream ends and we allow it to be pre-stretched by prescribing nonzero axial displacements at the two ends. At $x^1 = 0$ and $x^1 = L/R_0$ we have $v^1 = \pm\varepsilon_U/2$, $v^2 = 0$, $v^3 = 0$ and $v^3_{,1} = 0$. $\varepsilon_U = U/R_0$ represents the pre-stretch of the tube whose length has been changed from L to $L + U$. The corresponding boundary conditions for the discrete displacements V^{ijk}, whose nodes j lie on the clamped ends are: $v^{1j1} = \pm\varepsilon_U/2$ and $V^{1j3} = V^{2j1} = V^{2j3} = V^{3j1} = V^{3j2} = V^{3j3} = V^{3j4} = 0$. The symmetry boundary conditions to be applied at $x^2 = 0$ and $x^2 = \pi/N_{\text{buckl}}$ are $v^1_{,2} = v^3_{,2} = 0$ and $v^2 = 0$. This leads to the following boundary conditions for the discrete displacements V^{ijk}, whose nodes j lie on these lines: $V^{1j3} = V^{1j4} = V^{2j1} = V^{2j2} = V^{3j3} = V^{3j4} = 0$. We insert (33) into (32) and split the integration over the shell midplane into a summation over the N elements and an integration over the local coordinates (s_1, s_2), i.e.

$$\sum_{E=1}^{N} \sum_{j,k=1}^{4} \left\{ \int_0^1 \int_0^1 (\phi_i \psi_{jk} + \phi_{i\alpha} \psi_{jk,\alpha} + \phi_{i\alpha\beta} \psi_{jk,\alpha\beta}) \sqrt{a}\, \mathcal{J}\, \mathrm{d}s_1\, \mathrm{d}s_2 \right\} \delta V^{iJ(j,E)k} = 0; \tag{37}$$

$\mathcal{J}$ is the determinant of the Jacobian of the mapping between the local coordinates (s_1, s_2) and the global coordinates (x^1, x^2),

$$\mathcal{J} = \frac{\partial x^1}{\partial s_1} \frac{\partial x^2}{\partial s_2} - \frac{\partial x^1}{\partial s_2} \frac{\partial x^2}{\partial s_1}. \tag{38}$$

The variations of those V^{ijk} which are not determined by the boundary conditions are arbitrary. This leads to the following set of nonlinear algebraic equations f_{ijk} for the unknown V^{ijk}

$$f_{ijk} = \sum_{E=1}^{N} \int_0^1 \int_0^1 \{(\phi_i \psi_{lk} + \phi_{i\alpha} \psi_{lk,\alpha} + \phi_{i\alpha\beta} \psi_{lk,\alpha\beta})|_{J(l,E)=j} \sqrt{a}\, \mathcal{J}\}\, \mathrm{d}s_1\, \mathrm{d}s_2 = 0. \tag{39}$$

Linear numbering of these equations transforms them into the form given in (31). These equations still contain the load terms, which have to be determined from the solution of the fluid equations. We evaluate the double integral over the elements using a 3×3 Gaussian integration; see, e.g., Becker *et al.* (1984). Therefore, the load terms only need to be evaluated at the Gauss points within each element. We solved the above set of equations with a Newton-Raphson method, using the displacement variables V^{ijk} as the unknowns. At every stage of the iteration, the values of the V^{ijk} determine the shape of the tube wall. This allows us to solve the fluid equations and to evaluate the load terms. Then the residuals of the f_{ijk} are determined. Finally, the values of the unknowns were updated using the standard Newton-Raphson technique. The Jacobian matrix

$$J_{(i,j,k)(I,J,K)} = \frac{\partial f_{ijk}}{\partial V^{IJK}} \tag{40}$$

was determined using forward finite differencing. A finite-difference step of $\Delta V^{ijk} = 1{\cdot}0 \times 10^{-4}$ was found to be optimal.

3.2. Numerical Solution of the Fluid Equations

Let us assume that the tube shape has been determined from the displacement field v^i and that its cross-section A is known as a function of the axial coordinate z. In any given cross-section $A(z)$ we determine the velocity field and the pressure gradient by solving Poisson's equation

$$\nabla^2 \hat{u} = 1, \tag{41}$$

subject to the no-slip boundary condition

$$\hat{u}\big|_{\partial A(z)} = 0. \tag{42}$$

A comparison of the linear equations (11) and (41) shows that the real velocity field, u_z, which fulfils (11) and the normalization condition (13), is $u_z = c\hat{u}$, where the factor c is given by

$$c = \left(\int_{A(z)} \hat{u} \, \mathrm{d}A \right)^{-1}. \tag{43}$$

The pressure gradient in this cross-section is

$$\frac{\partial p}{\partial z} = cq \frac{\pi R_0}{8L}. \tag{44}$$

The wall shear stress, τ_w, is obtained from the velocity field using (24). Finally, the pressure distribution, $p(z)$, along the tube is obtained by integrating the pressure gradient along the tube. We prescribe the fluid pressure at one z-coordinate (e.g. $p|_{z=0} = p_{\text{entry}}$).

For the solution of the coupled problem, we have to determine the fluid traction in a sufficient number of cross-sections to be able to interpolate the load terms onto the Gauss points on the tube wall. Let us denote the z-coordinates of these cross-sections

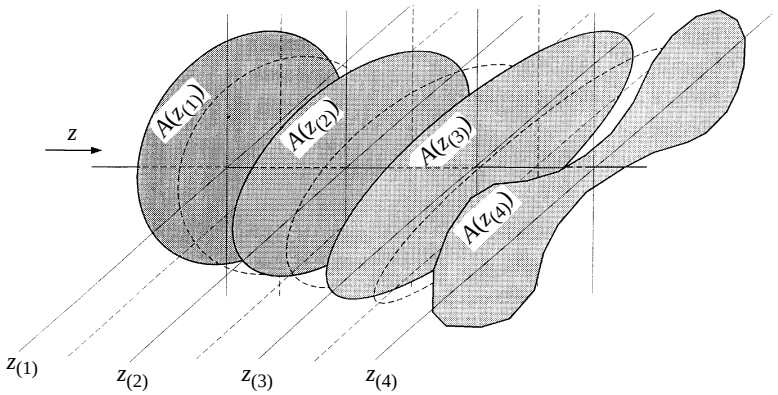

Figure 6. Illustration of the numerical scheme used to solve the fluid equations. The fluid traction is determined in the shaded cross-sections $A(z_{(i)})$. To integrate the pressure gradient numerically, additional solutions of the fluid equations are required in the dashed auxiliary cross-sections.

by $z_{(i)}$ $(i = 1, N_{\text{sect}})$. The solution strategy is illustrated in Figure 6. The solution of the equations (41) to (44) in the cross-sections $z = z_{(i)}$ determines the wall shear stress and the pressure gradient. To obtain the pressure distribution itself, we use a Gauss-Radau scheme to integrate the pressure gradient between these cross-sections. Hence, the pressure difference between two z-coordinates $z_{(i)}$ and $z_{(i+1)}$ is approximated by

$$p(z_{(i+1)}) - p(z_{(i)}) = \int_{z_{(i)}}^{z_{(i+1)}} \left(\frac{\partial p}{\partial z}\right) \mathrm{d}z \approx (z_{(i+1)} - z_{(i)}) \sum_{j=1}^{N_{\text{Radau}}} w_j \left(\frac{\partial p}{\partial z}\right)\Big|_{\hat{z}_j}, \tag{45}$$

where the integration points and weights for $N_{\text{Radau}} = 2, 3$ are given in Table 3 (Kopal 1955).

For $N_{\text{Radau}} = 3$ the numerical integration requires additional solutions of the equations (41) to (44) at $z = (z_{(i)} + z_{(i+1)})/2$ (dashed cross-sections in Figure 6). The fluid pressure at the upstream end of the tube provides the initial value for the pressure, $p(z_{(1)}) = p_{\text{entry}}$.

We solve Poisson's equation (41) numerically using a FEM technique. We decompose the cross-section $A(z)$ into triangular elements and interpolate the velocity field within element E as

$$\hat{u} = \sum_{j=1}^{3} U^{J(j,E)} \psi_j(s_1, s_2) \tag{46}$$

with the linear shape functions

$$\psi_1 = 1 - s_1 - s_2, \qquad \psi_2 = s_1 \qquad \text{and} \qquad \psi_3 = s_2. \tag{47}$$

TABLE 3

Integration points and weights for a Gauss–Radau integration with $N_{\text{Radau}} = 2$ and 3, respectively

j	$\hat{z}_j$	w_j	j	$\hat{z}_j$	w_j
1	$z_{(i)}$	1/2	1	$z_{(i)}$	1/6
2	$z_{(i+1)}$	1/2	2	$(z_{(i)} + z_{(i+1)}/2$	2/3
			3	$z_{(i+1)}$	1/6

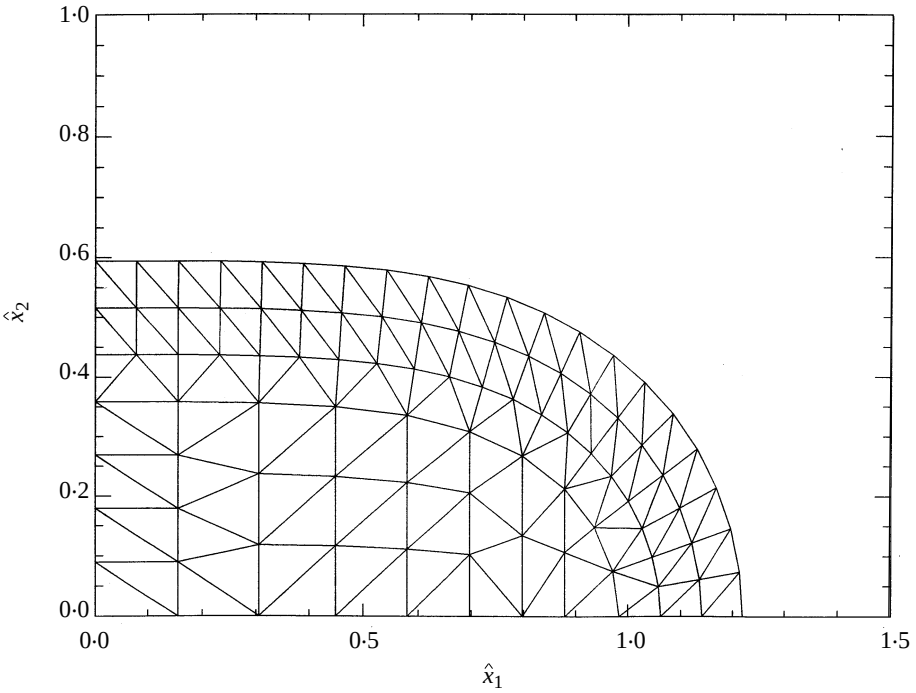

Figure 7. Finite element discretisation of a collapsing cross-section.

$J(j, E)$ stands for the global node number of local node j ($j = 1,3$) in element E. We solved (41) in Cartesian coordinates $(\hat{x}^1, \hat{x}^2) = (R_{\text{tube}} \cos \varphi, R_{\text{tube}} \sin \varphi)$. Again, only the relevant fraction of the cross-section was discretized (see Figure 7 for a $N_{\text{buckl}} = 2$ buckling mode).

To generate isoparametric elements, the mapping from the local coordinates (s_1, s_2) to the global coordinates $(\hat{x}^1, \hat{x}^2)$ within element E was chosen as

$$\hat{x}^\alpha = \sum_{j=1}^{3} \hat{X}^{\alpha J(j,E)} \psi_j(s_1, s_2), \tag{48}$$

where $\hat{X}^{\alpha J}$ stands for the coordinates $\hat{x}^\alpha$ of the node with global node number J. We use the standard Galerkin method which can be found in any textbook on the finite element method [see, e.g., Becker *et al.* (1984)] to transform (41) into

$$\sum_{E=1}^{N} \sum_{j=1}^{3} \int_{\Delta_E} \left(\frac{\partial \psi_i}{\partial \hat{x}^\alpha} \frac{\partial \psi_j}{\partial \hat{x}^\alpha} U^{J(j,E)} - \psi_i \right) \mathcal{J} \, ds_1 \, ds_2. \tag{49}$$

In this equation, the integration over the cross-section, $A(z)$, has been split up into a summation over the N elements and an integration over their areas Δ_E. $\mathcal{J}$ is the determinant of the Jacobian of the isoparametric mapping (48), i.e.

$$\mathcal{J} = \frac{\partial \hat{x}^1}{\partial s_1} \frac{\partial \hat{x}^2}{\partial s_2} - \frac{\partial \hat{x}^1}{\partial s_2} \frac{\partial \hat{x}^2}{\partial s_1}. \tag{50}$$

The area integrals over the elements in (49) were evaluated using a one-point Gauss

rule [integration point at $s_1 = s_2 = 1/3$ and weight $w = 1/2$; see Becker *et al.* (1984)]. The no-slip boundary condition prescribes zero velocities at nodes on the tube wall. The remaining velocities are obtained from (49) which is a system of linear equations for the unknown U^J. Its system matrix is sparse, symmetric and positive definite. Therefore, the system was solved with a banded Cholesky solver.

Due to the linear velocity interpolation in the elements, the volume flux through each element is equal to the area of the element, Δ_E, times the average of its nodal velocities. Since only a fraction of the cross-section was discretized, the normalization factor, c, is

$$c = \left(\int_{A(z)} \hat{u} \, \mathrm{d}A \right)^{-1} = \left(2N_{\mathrm{buckl}} \sum_{E=1}^{N} \frac{\Delta_E}{3} \sum_{j=1}^{3} U^{J(j,E)} \right)^{-1}, \tag{51}$$

where N_{buckl} is the circumferential buckling wavenumber. This determines the velocity field $u_z = c\hat{u}$ and the pressure gradient, using (44).

The only complication in the FEM solution of (41) is the need to provide an automatic mesh generator to decompose the possibly strongly collapsed cross-section into triangular finite elements. The coordinates of points on the tube wall are the only input that can be provided from the solid solver. Figure 7 shows how this problem was solved: given the z-coordinate of the cross-section, the $\hat{x}^\alpha$ coordinates of $2K + 1$ points on the tube wall are determined using the transformations (25) to (27) and an interpolation routine described in the next section. The distance between these points is $\hat{h} \approx \pi/(2N_{\mathrm{buckl}}K)$. We approximate the vector normal to the tube wall by the average of the normals to the two lines linking each boundary point to its neighbours (see Figure 8). Then the normals on all boundary points are used as spines to fill two rings of height $\hat{h}$ with elements. A third ring is added to link the two outer rings to the mesh in the central part of the cross-section, where vertical lines form the spines on which the mesh is generated. For strongly collapsed cross-sections, the height of the rings has

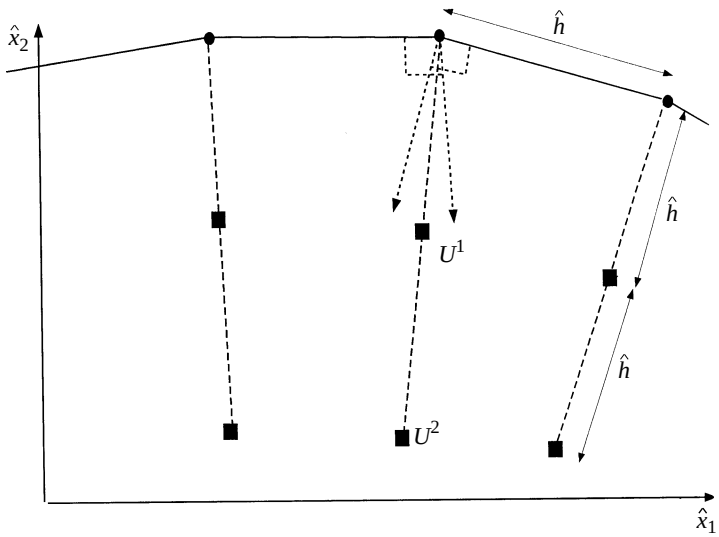

Figure 8. Sketch of the construction of the normal vector on the tube wall. The normal vectors are used as spines to generate the nodal points (marked by squares) of the two outer rings in the FEM mesh. The normal derivative of the velocity on the boundary points (marked by circles) is determined by backward differencing along the normals, using the velocities U^1 and U^2.

to be adjusted such that no nodal points are generated below the level $\hat{x}^2 = 0$. This is also necessary if the wall curvature is so large that the spines on the tube wall intersect. For the higher buckling wavenumbers, a triangular area near the origin has to be discretized separately (see Figure 19).

Once the velocity field has been computed, the normal derivative of the velocity is determined at all boundary points to obtain the wall shear stress (24). We used second order backward differencing along the normals on the boundary points (see Figure 8) to approximate the normal derivative, i.e.

$$\frac{\partial u_z}{\partial n} \approx \frac{4U_1 - U_2}{2\hat{h}}, \tag{52}$$

where the no-slip boundary condition has been used.

3.3. Fluid-Solid Coupling

As described in the foregoing, the solution of the coupled problem is essentially based on the FEM solution of the shell equations. The fluid solver merely serves to determine the load terms in these equations as a function of the wall displacement. In the solid-FEM code, the load terms need to be evaluated at the Gauss points on the tube wall. We solve the fluid equations in N_{sect} equally spaced cross-sections $z_{(i)}$, $i = 1, N_{\text{sect}}$ and then interpolate the fluid traction onto the solid Gauss points on the tube wall.

To obtain the Eulerian coordinates of the boundary points in the cross-sections $z = z_{(i)}$ from the transformations (26) and (27), we first have to determine their Lagrangian coordinates x^α. Since the tube wall deforms with little extension, we place the boundary points at $x^2_{(j)} = (\pi/N_{\text{buckl}})(j-1)/(2K)$, $j = 1, (2K+1)$. Thus the boundary points are approximately equally spaced in the circumferential direction. With these x^2-values, the transformation $z = z(x^1, x^2)$ given by (25) only depends on x^1. Hence, we determine the Lagrangian x^1-coordinate, $x^1_{(ij)}$, of the jth boundary point in the cross-section $z = z_{(i)}$ by solving

$$z(x^1_{(ij)}, x^2_{(j)}) - z_{(i)} = 0, \qquad j = 1, (2K+1) \tag{53}$$

for $x^1_{(ij)}$. We solved these equations using Ridder's method; see Press *et al.* (1992). Inserting the Lagrangian coordinates $(x^1_{(ij)}, x^2_{(ij)})$ of the boundary points into the transformations (26) and (27) establishes their Eulerian coordinates and enables us to generate the fluid meshes in these cross-sections. The z-coordinates of the auxiliary cross-sections, needed for the Gauss-Radau integration of the pressure gradient, are obtained from Table 3 and their meshes are generated in the same way.

Now, we use the procedure described in the previous section to determine the fluid traction in the N_{sect} cross-sections and then interpolate it onto the Gauss points. The fluid traction is known at the boundary points which lie on lines $z = z_{(i)}$ and $x^2 = x^2_{(j)}$. Since the pressure is a function only of z, we interpolate it quadratically, based on the z-coordinates of the Gauss points and the z-coordinates and the pressure values of three neighbouring cross-sections. The wall shear stress, τ_w, needs to be interpolated in the circumferential direction as well. The lines along which we distributed the boundary points in the circumferential direction, remain approximately perpendicular to the z-axis as the tube deforms. Therefore, we based the interpolation in the circumferential direction on the x^2-coordinates of the boundary points and that of the

Gauss points. Linear interpolation in this direction proved to be sufficient. In the axial direction we used the same quadratic interpolation as for the pressure.

3.4. The Continuation Technique

Due to the strong nonlinearity of the coupled problem, an efficient continuation technique is required to compute the deformation of the strongly collapsed tube. We need to be able to start the computation with parameter values corresponding to small deformations of the tube and then compute the larger deformations by a stepwise increase in one of the governing parameters (e.g. the volume flux). As will become clear later, the continuation technique has to be able to handle limit points (corresponding to a snap-through) and bifurcations. A general algorithm for such a continuation technique has first been proposed by Keller (1977). We used a simplified version of Keller's arclength method, known in the solid mechanics literature as a "displacement control technique" [see, e.g., Crisfield (1981) or Riks (1979)]. Let us assume that we base the continuation technique on a stepwise increase of the volume flux q. Then the deformation of the tube is described by a system of equations of the form $\mathscr{S}_i(\mathscr{V}_j, q) = 0$, $i, j = 1, N_{\mathrm{FEM}}$, and we compute the displacement field as a function of the volume flux, i.e. $\mathscr{V}_j = \mathscr{V}_j(q)$. If the increase δq during the parameter incrementation is small enough, then the solution $\mathscr{V}_j(q)$ will be a good initial guess for the Newton-Raphson iteration for the next solution $\mathscr{V}_j(q + \delta q)$. However, if the tube buckles with a snap-through (i.e. if there is a jump in the solution $\mathscr{V}_j$ at a critical value q_{crit}), then this continuation technique will generally fail at q_{crit}. To overcome this problem we augment the system of equations by an additional equation which prescribes the value of the $\hat{i}$th displacement variable, i.e.

$$\mathscr{S}_{N_{\mathrm{FEM}}+1} = \mathscr{V}_{\hat{i}} - \hat{\mathscr{V}} = 0, \tag{54}$$

where $\hat{\mathscr{V}}$ is at our disposal. With this additional equation we can regard the volume flux, q, as one of the unknowns. We chose $\mathscr{V}_i$ as the radial displacement of a node in the collapsing part of the tube. This allowed us to increment $\hat{\mathscr{V}}$ monotonically. While this method enables us to trace the deformation past limits points (snap-through) it does not necessarily switch from the unstable axisymmetric deformation onto the buckled path when the critical value of the volume flux is exceeded. Therefore, we forced the solution onto the buckled path by superposing a small nonaxisymmetric disturbance to the internal pressure distribution, p_{fluid}, i.e.

$$p = p_{\mathrm{fluid}} + p_{\cos} \cos(N_{\mathrm{buckl}} x^2). \tag{55}$$

We used $p_{\cos} = 1{\cdot}0 \times 10^{-5}$ and traced the solution path with this value until the deformation had reached the buckled regime where the disturbance is no longer needed to maintain the nonaxisymmetric deformation. Then we set the disturbance pressure to zero and proceeded with the continuation. An example of this procedure is illustrated in Figure 10.

The step-size for the displacement increment $\delta\hat{\mathscr{V}}$ was controlled by monitoring the number of iterations in the Newton-Raphson iteration required to achieve convergence (Crisfield 1981). We required an optimum number of iterations (usually four or five) and reduced or increased the stepsize $\delta\hat{\mathscr{V}}$ according to the ratio of the actual and optimal number of iterations needed for the previous step. If the iteration diverged or

failed to achieve convergence within 15 iterations, the step-size was reduced by a factor of two and the iteration was automatically restarted with the last converged solution.

If the Newton-Raphson procedure converges, it generates a sequence of displacement fields which approach the equilibrium configuration. However, the convergence is generally not monotonic and, especially for strongly collapsed tubes, the iteration can produce intermediate displacement fields in which the tube walls intersect. Wall contact or wall intersection were detected by monitoring the $\hat{x}^2$-values of the boundary points needed for the generation of the fluid mesh. If wall contact or an intersection was detected (i.e. if a boundary point was located at $\hat{x}^2 \leq 0$), then the Newton-Raphson correction for the displacement field was reduced until the wall contact was avoided.

It is not known *a priori* at which point on the tube wall opposite-wall contact occurs for the first time in the equilibrium configuration. Generally this point does not coincide with any FEM node. Hence, the radial displacement $\hat{V}_c$ at the control node when the first opposite wall contact occurs can be less than $1 - h/(2R_0)$.

If the continuation procedure sets the control displacement $\tilde{V}$ to a value larger than $\hat{V}_c$, then the Newton-Raphson iteration fails to converge since the displacement corrections are immediately reduced to avoid the opposite-wall contact. Following the non-convergence, the stepsize control mechanism reduces the displacement increment $\delta\hat{V}$ until a value $\tilde{V} < \tilde{V}_c$ is prescribed.

3.5. Discussion of the Numerical Solution and Validation of the Code

The code was developed on a Silicon Graphics Challenge XL computer with four R4400 processors and it was specifically designed for parallel processing. The most important feature of the implementation is the determination of the elements of the Jacobian matrix in parallel mode (CPU time reduced to about 28% of that of the serial version when running on four processors).

It should be noted that the fluid–solid interaction leads to a nonsymmetric and dense Jacobian matrix. This can easily be seen from the following argument: instead of using the variational principle (32), the system of equations (39) could have been derived by an examination of the local balance of internal and external forces. In this sense, the functions f_{ijk} are a measure of the imbalance between the generalized internal and external forces associated with the generalized displacements V^{ijk}. Therefore, the coefficient $J_{(i,j,k)(I,J,K)}$ represents the change in the force imbalance f_{ijk} due to a small change in the generalized displacement V^{IJK}.

Without fluid flow, the change in one of the discrete generalized displacements V^{ijk} only affects the balance of forces in the four elements sharing the node j. This is due to the particular choice of shape functions in the FE method. Their finite support leads to a sparse band structure of the Jacobian matrix. In this case the Jacobian matrix is also symmetric and positive definite as can be deduced from the conservation of energy (the elastic system alone is conservative).

To examine the case with through flow, let us assume that the pressure at the upstream end of the tube is prescribed. Then the pressure distribution is obtained by integrating the pressure gradient (11) in the downstream direction. This implies that changes in the discrete displacements at one point affect the pressure distribution (and therefore the local balance of forces) everywhere downstream of this point, whereas the pressure upstream of this point remains unaffected. This mechanism couples upstream and downstream degrees of freedom and leads to an asymmetric and rather dense Jacobian matrix. Physically, the asymmetry corresponds to the fact that the elastic system can now gain energy from the fluid flow.

The asymmetry of the Jacobian matrix increases the computational cost considerably. Firstly, a substantially larger number of entries in the Jacobian matrix has to be computed. Secondly, the linear system to be solved during the Newton-Raphson iteration has to be solved using LU decomposition. This is much slower than the banded Cholesky solver which can be used for the symmetric positive definite matrix of the no-flow case.

To validate the code we carried out a number of tests. To test the fluid solver and the transformations between the Lagrangian and Eulerian coordinate systems, we determined a displacement field v^i which deformed the tube cross-sections into ellipses. The z-dependence of the cross-sections was chosen such that the pressure distribution could be determined by integrating (11) analytically. The scheme described in Section 3.2 was found to be very accurate even for strongly deformed cross-sections, extreme stretching of the tube wall and for FEM meshes which consist of elements of very different sizes.

A consistency check for the numerical values of the wall shear stress and the pressure gradient in the cross-sections is derived by applying Gauss' theorem to equation (11) which thereby takes the form

$$q\frac{\pi R_0}{8L}\oint_{\partial A}\frac{\partial u_z}{\partial n}\,\mathrm{d}S=\oint_{\partial A}\tau_w\,\mathrm{d}S=A\frac{\partial p}{\partial z}, \tag{56}$$

where the contour integral has to be evaluated along the boundary of the cross-section. This equation states the balance of forces between the wall shear stress and the pressure gradient in the cross-section $A(z)$. Both sides can easily be evaluated during the FEM solution of (11). For the discretizations used in our computations the difference between the two sides of the equation was less than 0·1%.

The solid solver was tested by comparing the numerical and analytical solutions for small nonaxisymmetric deformations under given external loads [for small external loads, the tube deformation is governed by the linearized shell equations which can be solved analytically; see, e.g., Schnell & Eschenauer (1984)]. For large axisymmetric deformations, the numerical solutions were compared to those obtained by using our axisymmetric code (Heil & Pedley 1995). We also compared the tube deformation under constant external pressure and with boundary conditions corresponding to that of an infinitely long tube to the (unpublished) results obtained by using a FEM code designed to investigate the post-buckling of rings. This case was also compared to Flaherty, Keller & Rubinow's (1972) inextensional post-buckling analysis. In all cases we obtained excellent agreement between the results. Finally, we compared the critical buckling parameters to the predictions of Heil's (1995a) linear stability analysis. The critical values for the volume flux differed by less than 3% (see Table 4, to be discussed later).

Various discretizations of the tube wall and the fluid domain were used to check for convergence. Most computations were carried out with 4×9 shell elements in the circumferential and axial direction, respectively. The mesh spacing was denser near the supports and in the strongly collapsed part of the tube (in the figures the element boundaries are shown by solid lines on the tube wall). The fluid domain was discretized with $N_{\mathrm{sect}}=40$ equally spaced cross-sections and the meshes in the cross-section were generated with $2K+1=15$ boundary points. The Gauss–Radau integration was performed with $N_{\mathrm{Radau}}=2$.

The main computational cost is associated with the determination of the elements of the Jacobian matrix. For a typical discretization, the set-up of the Jacobian matrix required about 400 s of CPU time.

4. RESULTS AND DISCUSSION

The nondimensional parameters used for the computation presented in this paper are $h/R_0 = 1/20$, $L/R_0 = 10$ and $\nu = 0{\cdot}49$. This corresponds to nondimensional bending and membrane stiffnesses of

$$K_{\text{bend}} = \frac{1}{12(1-\nu^2)}\left(\frac{h}{R_0}\right)^3 = 1{\cdot}37 \times 10^{-5} \tag{57}$$

and

$$D_{\text{membr}} = \frac{1}{1-\nu^2}\frac{h}{R_0} = 6{\cdot}57 \times 10^{-2}. \tag{58}$$

Poisson's ratio and the relative wall thickness were chosen to be in the range of parameters in the experiments of Elad *et al.* (1992), where (by the standards of shell theory) relatively thick-walled rubber tubes had been used. The effects of changes in the tube geometry are discussed below. In all cases the external pressure was set to zero, $p_{\text{ext}} = 0$, and transmural pressure differences were generated by adjusting the fluid pressure.

To illustrate the mechanism which leads to the buckling of the tube, let us assume that we keep the upstream pressure, p_{entry}, constant while we increase the volume flux. For a rigid tube, an increase in the volume flux increases the viscous pressure drop; therefore, the compressive load on the tube wall increases with the axial distance from the upstream end. If the tube is elastic, the corresponding deformation reduces the cross-sectional area of the tube, which increases the pressure drop even further. For small values of the volume flux, the tube deforms axisymmetrically until a critical value of the compressive load is reached. At this critical value, the axisymmetric deformation becomes unstable and the tube buckles nonaxisymmetrically. It is a characteristic feature of thin shell structures that their membrane stiffness is much larger than their bending stiffness. The axisymmetric pre-buckling deformation is accompanied by circumferential membrane strains, which make the tube relatively stiff. After the buckling, the membrane stiffness contributes very little to the overall stiffness of the tube [the buckling of circular rings or infinitely long cylindrical tubes can be analysed very accurately under the assumption of inextensibility, which neglects the membrane effects completely; see e.g. Flaherty *et al.* (1972)]. Hence, the post-buckling deformations of the tube are very large and the change in the tube stiffness during the buckling is so drastic that the tubes typically buckle with a snap-through. [The buckling of cylindrical shells under hydrostatic pressure has received far less attention than the buckling under axial loads. However, excellent accounts of some experimental investigations into the problem can be found in Esslinger & Geier (1971), Thielemann & Esslinger (1967) and Kirstein & Wenk (1956), for example].

To illustrate the buckling behaviour of the tube without fluid–solid coupling, we first examine the deformation of a cylindrical shell, subject to a prescribed load given by

$$p(z) = p_{\text{entry}} - \left(\frac{R_0}{L}\right)\frac{qz}{(1-h/2R_0)^4} \quad \text{and} \quad \tau_w = -\frac{1}{2}\frac{R_0}{L}\frac{q}{(1-h/2R_0)^3}. \tag{59}$$

This load corresponds to the traction exerted by the fluid flow on the undeformed tube wall. Thus, the interaction between the fluid traction and the wall deformation is neglected.

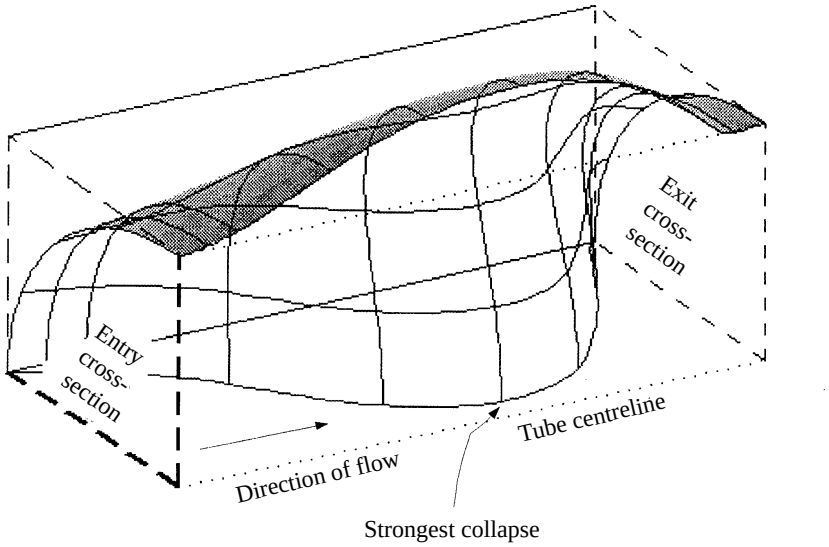

Figure 9. Post-buckling deformation of a tube without fluid–solid coupling. Only one quarter of the tube is shown. $L/R_0 = 10$, $p_{\text{entry}} = 0$, $q = 2{\cdot}0 \times 10^{-4}$.

Figure 9 shows the buckled tube subject to this load for $q = 2{\cdot}0 \times 10^{-4}$. The central part of the tube is strongly collapsed. Due to its high membrane stiffness, the tube buckles with little circumferential extension. Therefore, the material line $x^2 = 0$ bulges out while the material line $x^2 = \frac{1}{2}\pi$ collapses towards the centreline (see Figure 5 for the coordinates used). In spite of the asymmetric load in the axial direction, the buckling deformation is approximately symmetric; the point of the strongest collapse is near $x^1 = L/(2R_0)$.

Figure 10 shows the corresponding bifurcation diagram: the radial displacements of two material points on the tube wall (at $x^1 = 7{\cdot}4$ and $x^2 = 0,\ \pi/2$) are plotted against

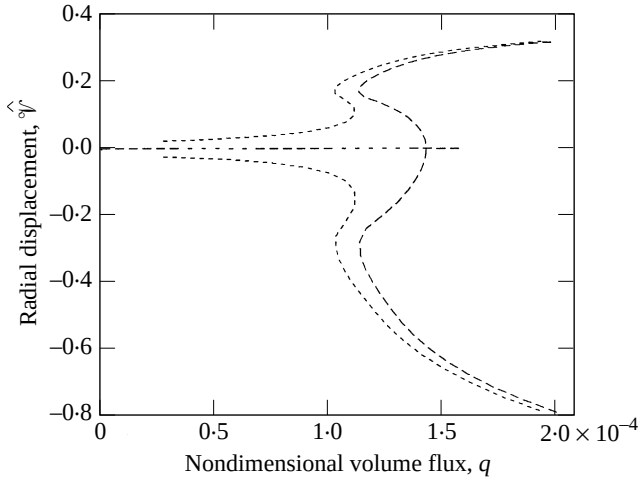

Figure 10. Bifurcation diagram for the tube without fluid–solid coupling. The radial displacements of two material points at $x^1 = 7{\cdot}4$ and $x^2 = 0,\ \frac{1}{2}\pi$ are plotted against the volume flux, q. Dash-dotted line: axisymmetric pre-buckling deformation; dashed line: post-buckling deformation; short-dashed line: deformation if a small nonaxisymmetric disturbances $p_{\cos}\cos(2x^2)$ is superimposed on the fluid traction; $p_{cos} = 1{\cdot}0 \times 10^{-5}$.

the nondimensional "volume flux" q. The dash-dotted line represents the axisymmetric pre-buckling deformation of the tube for an upstream pressure of $p_{\text{entry}} = 0$. For zero "volume flux", the tube wall is load-free and the radial displacements of the material points are equal to zero. As the "volume flux" increases, the tube wall is subject to an increasing compressive load. Since the tube pre-buckling stiffness is very high, the pre-buckling curve has a very small negative slope, indicating the compression of the tube as the "volume flux" increases. At $q = 1{\cdot}44 \times 10^{-4}$ the axisymmetric deformation becomes unstable and the tube buckles nonaxisymmetrically with a circumferential buckling wavenumber $N_{\text{buckl}} = 2$. The material point at $x^2 = 0$ moves radially outwards, while the material point at $x^2 = \pi/2$ collapses towards the centreline. The bifurcation is subcritical and the tube buckles with a snap-through: the reduction in the tube stiffness after the buckling is so significant that the bending moments, needed to balance the critical load in the non-axisymmetric configuration, can only be generated by large deformations. At a "volume flux" of $q = 2{\cdot}01 \times 10^{-4}$ the tube deformation is so large that opposite-wall contact occurs at some point on the tube wall.

The short-dashed lines in Figure 10 show the equilibrium paths if a small nonaxisymmetric disturbance $p_{\cos} \cos(N_{\text{buckle}} x^2)$ is superimposed on the pressure distribution given by (59). The small nonaxisymmetric load is significant only in the vicinity of the buckling point. In the computations, the tube was forced into the buckled configuration by following this path until the buckling was sufficiently strong. Then the nonaxisymmetric disturbance was switched off and the Newton-Raphson iteration continued on the undisturbed post-buckling path, which was traced back to the bifurcation point.

Figure 9 shows that the buckling reduces the tube cross-sectional area and thereby increases its resistance significantly. The resistance has its highest value in the most strongly collapsed central part of the tube.

Figure 11 shows how the tube buckling affects the pressure distribution when the change in the flow after the buckling is taken into account. The solid line represents the prescribed pressure distribution which keeps the tube in a buckled configuration which

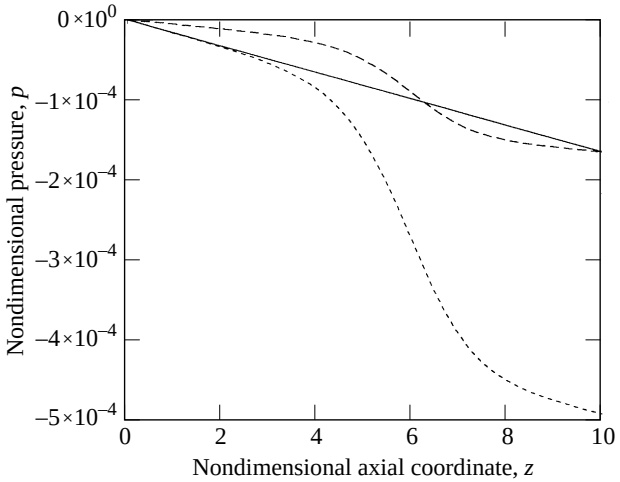

Figure 11. Pressure distributions through a tube which is held in a stable buckled configuration by a prescribed pressure distribution (solid line). This pressure distribution corresponds to a "volume flux" of $q = 1{\cdot}44 \times 10^{-4}$ in the undeformed tube. The short-dashed line shows the pressure distribution induced by a real flow ($q = 1{\cdot}44 \times 10^{-4}$) through the buckled tube (but without any changes in the tube shape). The dashed line is the pressure distribution induced by a real flow if the pressure drop through the tube is fixed.

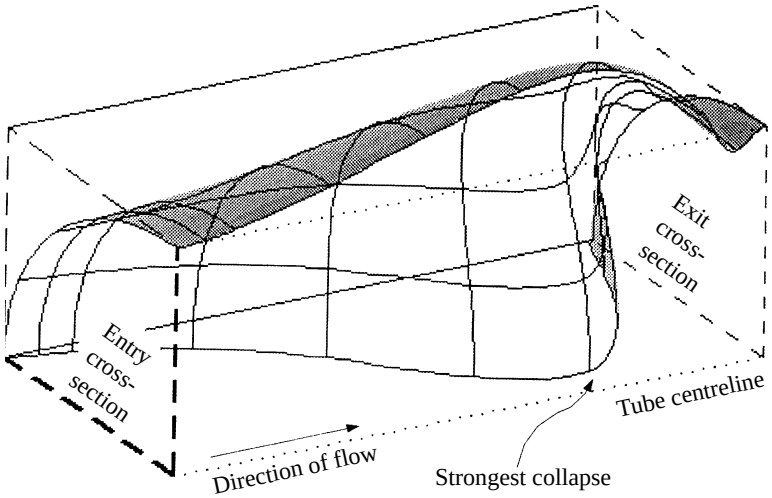

Figure 12. Strongly collapsed tube subject to $p_{ext} = p_{entry} = 0$ and a volume flux of $q = 4{\cdot}75 \times 10^{-5}$; $L/R_0 = 10$.

is similar to the one shown in Figure 9. If we keep the wall shape constant and subject the tube to a real flow with the same value of the volume flux q, the increased resistance in the central part of the tube induces a strongly increased compressive load on the tube wall (short-dashed line). The dashed line shows the pressure distribution in the tube if we subject it to a real flow which gives rise to the same pressure drop $p_{entry} - p_{exit}$ as the prescribed load. In this case, the increased resistance reduces the volume flux and re-distributes the pressure drop: the compressive load acting on the upstream part of the tube is reduced while the load on the downstream part is increased slightly.

Figure 12 shows the deformation of the tube when the full fluid–solid coupling is taken into account. The increased resistance of the tube after buckling moves the point of strongest collapse towards the downstream end. Figure 13 shows that the tube collapses most strongly (cross-sectional area reduced to about 35% of the original value) at about 75% of its length. The plot of the pressure distribution in Figure 13 clearly shows the additional pressure drop in the strongly collapsed part of the tube (the initial slope of the curve indicates the pressure drop through the undeformed tube for the same volume flux).

Figure 14 shows the velocity distribution in two cross-sections at 42% and 63% of the tube length. The dashed lines within the cross-sections represent the isolines of the axial velocity u_z. The spikes on the tube wall indicate the magnitude of the wall shear stress, τ_w, at the boundary points. At 42% of the tube length the cross-section is nearly elliptical, therefore the maximum velocity is reached on the tube centreline and the wall shear stress has its maximum value at the narrowest point of the cross-section. In the strongly collapsed cross-section at 63% of the tube length, the flow begins to split up into two branches as the opposite walls move closer together. As less fluid passes through the central part of the cross-section, the point of maximum wall shear stress moves away from the narrowest point towards the point of the maximum velocity where the velocity gradients are higher. The wall shear stress is significantly increased in the strongly collapsed cross-section (the scale for the wall shear stress is the wall shear stress on the undeformed tube wall).

Figure 11 already indicated that the post-buckling behaviour of the tube with

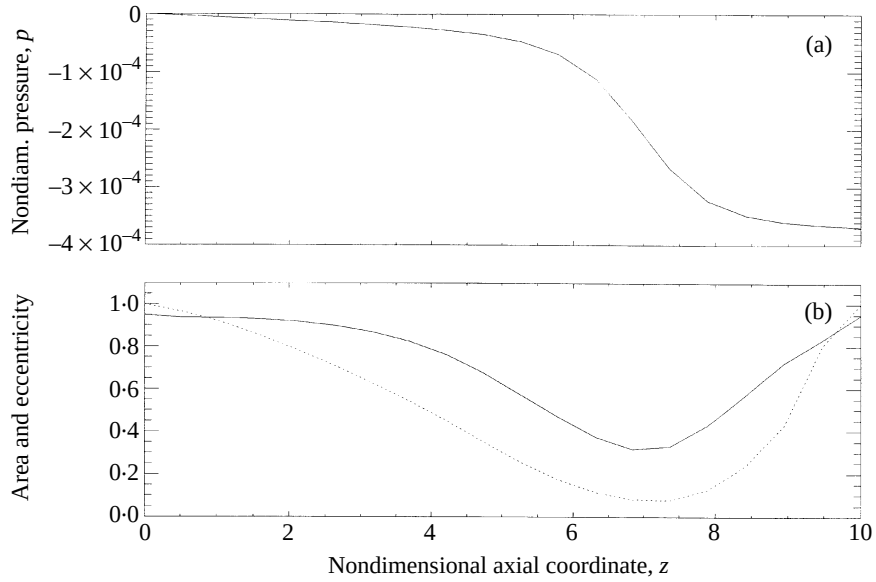

Figure 13. (a) Pressure distribution and (b) nondimensional cross-sectional area, $A/(\pi R_0^2)$, (solid line) and eccentricity (dotted line) of the collapsed tube. The eccentricity is defined as the width to height ratio of the cross-section. Parameters as in Figure 12.

fluid–solid coupling depends strongly on which one of the two control parameters (volume flux or pressure drop through the tube) is kept constant during buckling.

A constant volume flux during buckling could be realized experimentally with a volumetric pump at the downstream end of the collapsible tube while the upstream end is fed from a constant head reservoir. The increased pressure drop, induced by the buckling will then increase the compressive load on the downstream end of the tube and accelerate its collapse. The bifurcation diagram for this case is shown in Figure 15. The short-dashed line stands for the axisymmetric pre-buckling deformation, the solid line is the post-buckling curve with full fluid–solid coupling and the dashed line is the post-buckling curve without fluid–solid coupling, as shown before in Figure 10. The diagram shows that the fluid–solid coupling slightly reduces the value of the volume flux at which the axisymmetric deformation of the tube becomes unstable. This is because the axisymmetric pre-buckling deformation already reduces the cross-sectional area of the tube and thereby increases the tube resistance. Hence, for a given volume flux, the compressive load induced by the flow through the deformed tube is higher than that induced by the flow through the undeformed tube.

The difference in the post-buckling paths is far more significant. While the bending moments generated by the large post-buckling displacements are sufficient to balance a dead load, they are too small to balance the drastic increase in the compressive fluid load after the buckling. The unstable post-buckling path can be traced to the point where opposite-wall contact occurs at some point in the tube. Physically, the tube would immediately buckle into a configuration in which the opposite walls are in contact.

If the pressure drop through the tube is kept constant during buckling, then the pressure distribution changes as illustrated in Figure 11, i.e. the compressive load on the tube wall upstream of the point of strongest collapse is reduced, while the compressive load on the downstream part is increased slightly. With fluid–solid coupling, the point of strongest collapse moves towards the downstream end. Hence,

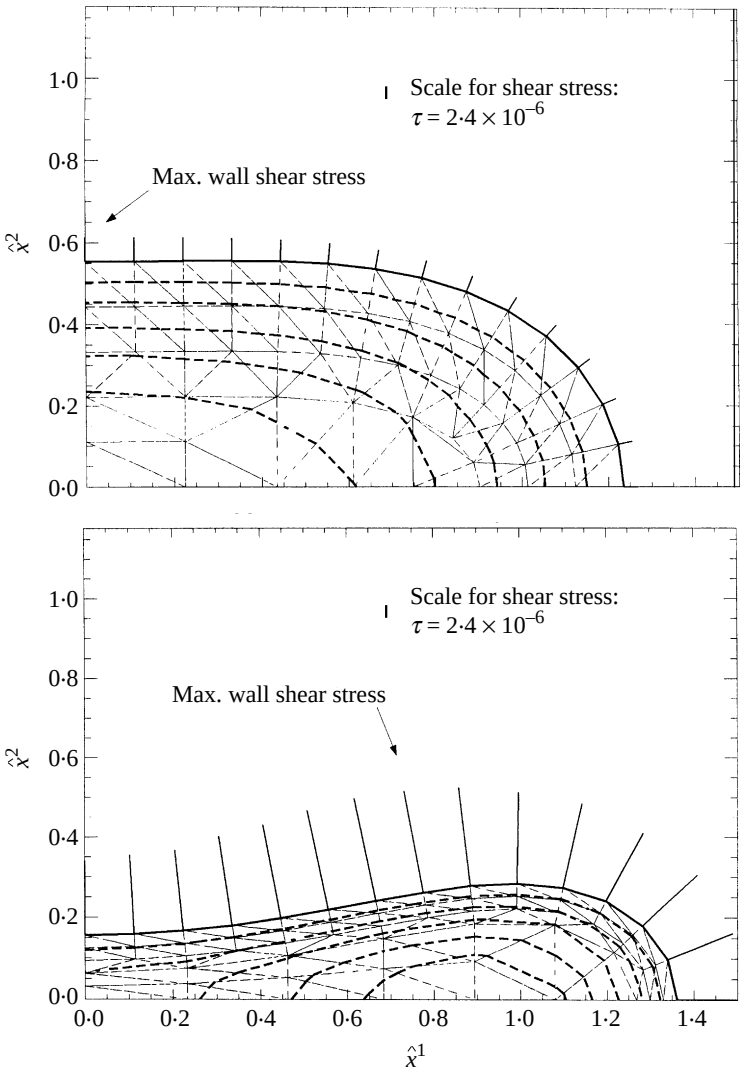

Figure 14. Fluid flow and wall shear stress in the cross sections at 42% and 63% of the tube length. The thin dashed lines show the FEM mesh. The velocity increment between the isovelocity lines (thick dashed lines) is constant. The spikes normal to the tube wall indicate the magnitude of the wall shear stress. The maximum axial velocities are $u_{z\max} = 0{\cdot}81$ and $u_{z\max} = 1{\cdot}80$ in the upper and lower figure, respectively. Parameters as in Figure 12.

only the small fraction of the tube downstream of the point of strongest collapse is subject to an increased compressive load, whereas the compressive load is reduced over most of the tube length. Therefore, the tube collapse is slowed down by the fluid–solid coupling. The corresponding bifurcation diagram (radial displacements of the same material points as in Figure 15 plotted against the pressure drop) is shown in Figure 16. It shows clearly that the axisymmetric deformation of the tube loses its stability when the compressive load has reached a certain critical value. The mechanism generating the compressive load (a viscous flow interacting with the pre-buckling deformation or a prescribed load) is irrelevant. However, with fluid–solid coupling, a substantially higher pressure drop is required to achieve the same level of collapse: without fluid–solid

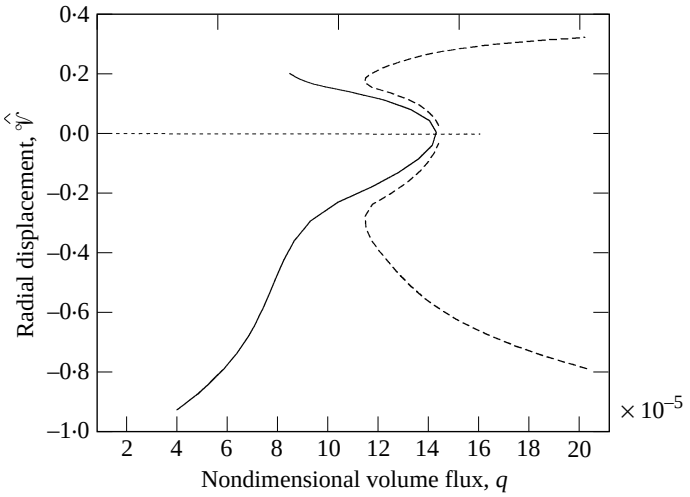

Figure 15. Bifurcation diagram with full fluid–solid coupling (solid line) and without fluid–solid coupling (dashed line). The radial displacements of two material points at $x^1 = 7{\cdot}4$ and $x^2 = 0$, $\frac{1}{2}\pi$ are plotted against the volume flux, q. The short-dashed line represents the axisymmetric pre-buckling deformation. $L/R_0 = 10$, $p_{ext} = p_{entry} = 0$.

coupling opposite-wall contact occurs for $p_{entry} - p_{exit} = 2{\cdot}23 \times 10^{-4}$; with fluid–solid coupling more than twice this value is required to collapse the tube to this extent.

The flow characteristics of the collapsible tube are shown in Figure 17. Before the buckling, the relation between pressure drop $\Delta p = p_{entry} - p_{exit}$ and volume flux is approximately linear: an increase in the pressure drop increases the volume flux. At point A the axisymmetric pre-buckling deformation loses its stability and the tube buckles. If the pressure drop is kept constant during the buckling, then the drastically increased flow resistance in the buckled tube reduces the volume flux approximately by a factor of two. After the buckling, the tube resistance increases so rapidly that any further increase in the pressure drop reduces the volume flux through the tube. This

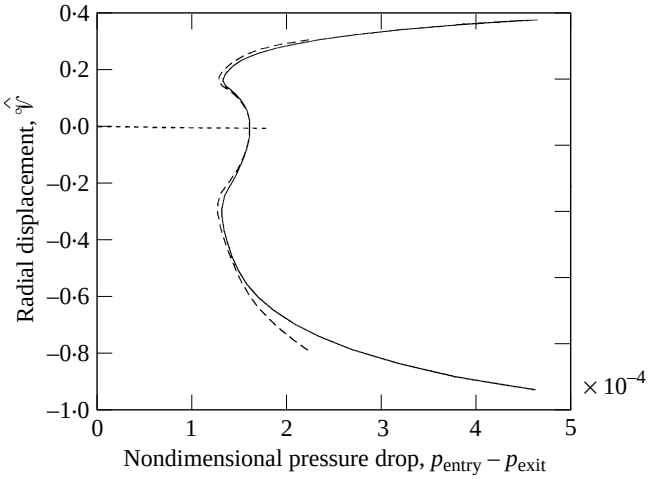

Figure 16. Bifurcation diagram with full fluid–solid coupling (solid line) and without fluid–solid coupling (dashed line). The radial displacements of two material points at $x^1 = 7{\cdot}4$ and $x^2 = 0$, $\frac{1}{2}\pi$ are plotted against the pressure drop $p_{entry} - p_{exit}$. The short-dashed line represents the axisymmetric pre-buckling deformation. $L/R_0 = 10$, $p_{ext} = p_{entry} = 0$.

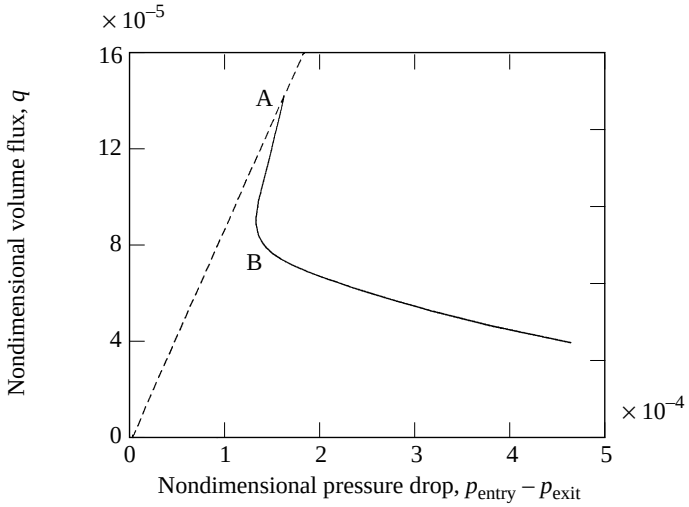

Figure 17. Volume flux q is a function of the driving pressure difference $p_{\text{entry}} - p_{\text{exit}}$ before (dashed line) and after (solid line) the buckling; $L/R_0 = 10$, $p_{\text{ext}} = p_{\text{entry}} = 0$.

behaviour is known as ''flow limitation'' or ''negative effort dependence'' (Kamm & Pedley 1989). The pressure drop/flow relationship between points A and B is multivalued and hysteresis can be observed: if the pressure drop is reduced from a value which is larger than Δp_{A} then the tube remains buckled until point B($\Delta p_B < \Delta p_A$) where the buckled tube snaps back into the axisymmetric configuration.

We investigated the effect of three parameters on the post-buckling behaviour; namely the upstream pressure, p_{entry}, the axial pre-stretch, ε_U, and the ratio L/R_0. We shall discuss the effects of changes in these parameters and illustrate them, where appropriate, with concrete results [Table 4 summarizes all parameter studies carried out; a detailed compilation of all results can be found in Heil (1995)].

First, we consider the case in which the upstream fluid pressure, p_{entry}, is increased to a positive value, such that the upstream end of the tube is subject to an outward pressure. In this case, the viscous pressure drop induced by the flow has to overcome the upstream pressurization before the downstream end is under a sufficiently strong compressive load to initiate the buckling. Also, since the upstream part of the tube remains distended, the tube resistance is smaller than that of an unpressurized tube. Therefore, the critical volume flux at which buckling occurs is increased by an increase in the upstream pressure. Furthermore, only the compressed downstream part of the tube actually participates in the buckling; therefore, the buckling is similar to the buckling of a shorter tube. This mechanism has already been analysed in the linear stability analysis (Heil 1996), where it was also shown that the most unstable wavenumber of the buckling mode increases with the upstream pressurization [shorter cylindrical tubes buckle with higher circumferential wavenumbers (Yamaki 1984)].

Figure 18 shows a buckled tube under high upstream pressure, $p_{\text{entry}} = 2 \times 10^{-3}$. Due to the upstream pressurization, only the last 25% of the tube length is involved in the buckling, and the tube buckles with $N_{\text{buckl}} = 4$ waves in the circumferential direction. For deformations with circumferential buckling wavenumbers $N_{\text{buckl}} > 2$, the entire circumference collapses towards the tube centreline when the buckling deformation becomes sufficiently large. This is again due to the high membrane stiffness of the tube: finite radial buckling displacements of the form suggested by the linear stability

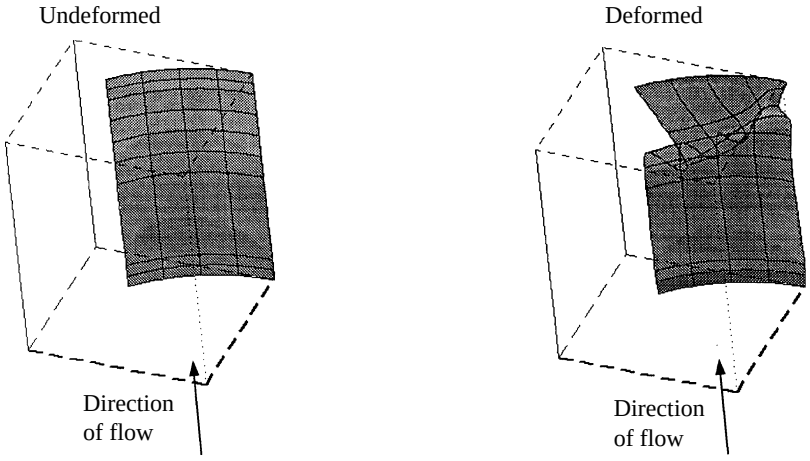

Figure 18. Deformation of a tube under high upstream pressure $p_{entry} = 2{\cdot}0 \times 10^{-3}$. Only one eighth of the tube is shown. $L/R_0 = 10$, $P_{ext} = 0$, $q = 1{\cdot}78 \times 10^{-3}$.

analysis, $v^3 \sim \cos(N_{buckl}\, x^2)$ with $N_{buckl} > 2$, would stretch the tube wall in the circumferential direction.

The fluid flow in a strongly collapsed cross-section of this tube, shown in Figure 19, is noticeably different from the flow through a cross-section which buckles with $N_{buckl} = 2$ circumferential waves. The fluid flow is concentrated near the tube centreline as the flow resistance in the outer lobes becomes too high. Again, the reduction in the cross-sectional area is accompanied by a significant increase in the wall shear stress and the pressure gradient.

The corresponding bifurcation diagram in Figure 20 shows that the viscous pressure drop in the strongly collapsed part of the tube increases the compressive load beyond a

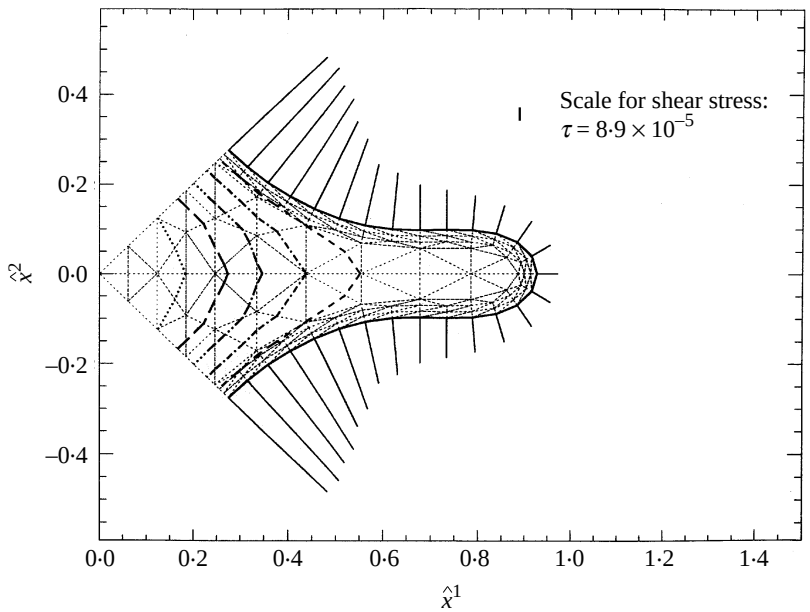

Figure 19. Flow through a strongly buckled cross-section at 87% of the tube length. The velocity increment between the isovelocity lines (thick dashed lines) is constant. $u_{zmax} = 2{\cdot}94$; other parameters as in Figure 18.

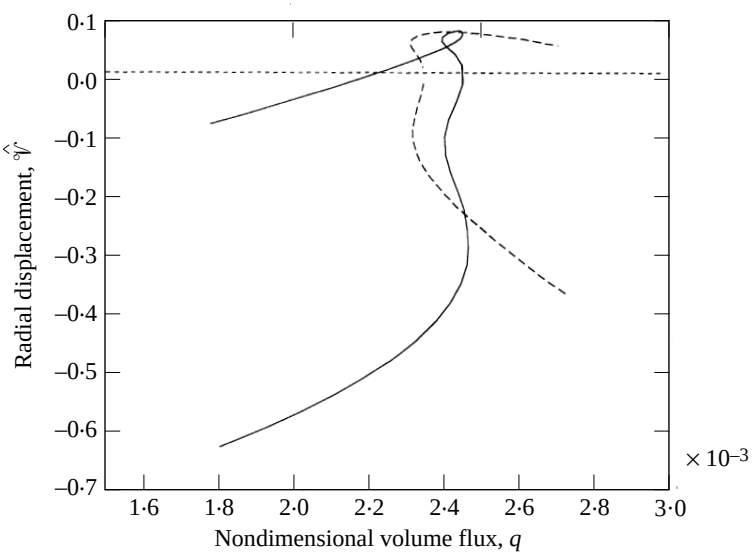

Figure 20. Bifurcation diagram for a tube with $L/R_0 = 10$, $p_{\text{entry}} = 2{\cdot}0 \times 10^{-3}$, $p_{\text{ext}} = 0$, $N_{\text{buckl}} = 4$. The positions of the material points traced are $x^1 = 9{\cdot}0$ and $x^2 = 0$, $\frac{1}{4}\pi$. Solid line: full fluid–solid coupling; dashed line: no fluid–solid coupling; short-dashed line: axisymmetric pre-buckling deformation.

level that can be balanced by the bending moments: the fluid–solid interaction still leads to immediate opposite-wall contact if the volume flux is kept at a constant value during the buckling. During the initial stages of the buckling, the increase in the bending moments is sufficiently strong to stabilize a short section of the post-buckling path (radial displacement between $\hat{\mathscr{V}} \approx -0{\cdot}12$ and $\hat{\mathscr{V}} \approx -0{\cdot}31$). The volume flux on this section of the path is less than the critical value q_{crit}, and sufficiently large disturbances could force the tube into this buckled configuration before the critical value of the volume flux is reached.

The bifurcation diagram shows that during the early stages of buckling, the buckling deformation is that predicted by linear theory: the material line $x^2 = 0$ bulges out, while the line $x^2 = \pi/4$ moves towards the centreline. However, as the amplitude of the deformation increases, the parts of the tube which were bulging out initially, are drawn towards the centreline as well and both branches of the bifurcation diagram have a negative slope.

As mentioned above, the upstream pressurization reduces the tube resistance (compared to a rigid tube). Therefore, the critical volume flux with full fluid–solid coupling (solid line) is higher than the critical volume flux without fluid–solid coupling (dashed line).

One could increase the upstream pressure to such an extent that only a very small fraction of the tube would buckle with very high circumferential wavenumbers. Large deformations of this type would be accompanied by strong stretching and bending of the tube wall. The wall stiffness might then be large enough to balance the compressive fluid load before opposite-wall contact occurs. However, such deformations would have little in common with the experimental observations in which most of the tube length is involved in the $N_{\text{buckle}} = 2$ buckling. Therefore, no attempts were made to investigate this parameter range.

The effects of axial pre-stretch on the pre-buckling deformation and on the stability of the tube were discussed in Heil & Pedley (1995) and Heil (1996a), respectively.

TABLE 4

Table of all parameter studies carried out. In all cases $h/R_0 = 1/20$ was used. q_{crit} is the critical value for the volume flux, obtained from the bifurcation diagrams. $q_{crit}^{(in)}$ is the value predicted by the linear stability analysis (Heil 1996)

Case no.	L/R_0	Axial pre-stretch U/L	p_{entry}	N_{buckl}	q_{crit}	$q_{crit}^{(lin)}$
1	5	0%	0	3	$2{\cdot}68 \times 10^{-4}$	$2{\cdot}68 \times 10^{-4}$
2	10	0%	0	2	$1{\cdot}42 \times 10^{-4}$	$1{\cdot}45 \times 10^{-4}$
3	10	0%	$1{\cdot}0 \times 10^{-3}$	3	$1{\cdot}35 \times 10^{-3}$	$1{\cdot}35 \times 10^{-3}$
4	10	0%	$2{\cdot}0 \times 10^{-3}$	4	$2{\cdot}46 \times 10^{-3}$	$2{\cdot}47 \times 10^{-3}$
5	10	5%	$5{\cdot}0 \times 10^{-4}$	3	$7{\cdot}76 \times 10^{-4}$	$7{\cdot}86 \times 10^{-4}$
6	10	5%	$2{\cdot}0 \times 10^{-3}$	4	$2{\cdot}33 \times 10^{-3}$	$2{\cdot}33 \times 10^{-3}$
7	20	0%	0	2	$6{\cdot}93 \times 10^{-5}$	$7{\cdot}09 \times 10^{-5}$
8	20	5%	$3{\cdot}5 \times 10^{-4}$	2	$5{\cdot}14 \times 10^{-4}$	$5{\cdot}19 \times 10^{-4}$

While axial pre-stretch generally increases the tube stiffness, its effect is not strong enough to stabilize the post-buckling deformation sufficiently to avoid immediate opposite-wall contact when the volume flux is kept constant during the buckling. Qualitatively, the post-buckling curves for buckling under constant volume flux remain unchanged by the axial prestretch. A 5% axial pre-stretch was, however, sufficient to change the subcritical bifurcations for buckling under constant pressure drop in cases 3 and 4 (see Table 4) into supercritical bifurcation (cases 5 and 6): the pre-stretched tubes buckle continuously without a snap-through.

Finally, we investigated the effect of changes in the geometrical parameters L/R_0 and h/R_0. Again, no significant changes in the post-buckling behaviour were found for buckling under constant volume flux. Very short tubes are the most likely candidates for a collapse without immediate opposite-wall contact, for the reasons described above. The wall thickness $h/R_0 = 1/20$ used in all computations is already at the upper limit of the applicability of the Kirchhoff-Love assumption. Nevertheless, one computation was carried out for a wall thickness of $h/R_0 = 1/10$, but the increased bending stiffness was still not high enough to stabilize the post-buckling deformation to such an extent that opposite-wall contact after buckling could be avoided.

Buckling under a constant pressure drop is influenced by a change in the tube length: for the longer tubes of cases 7 and 8 ($L/R_0 = 20$), the buckling is subcritical without fluid–solid coupling and supercritical with fluid–solid coupling. This can be explained as follows: the buckling of the tube stretches the wall axially (Figure 12 shows that the arclengths of the lines $x^2 = 0$ and $x^2 = \pi/2$ are increased by the buckling). For a given maximum radial displacement (opposite-wall contact at one point on the line $x^2 = \pi/2$, say), the relative extension of the tube wall increases as the buckling becomes more localized near the downstream end. This is illustrated in the sketch in Figure 21. The extension ratio for a symmetric collapse is

$$\left(\frac{l_{sym}}{L}\right)^2 \approx 1 + 4\left(\frac{R_0}{L}\right)^2, \tag{60}$$

where l is the arclength of the material line after the deformation. If the strongest collapse occurs at the downstream end, the extension ratio is

$$\left(\frac{l_{asym}}{L}\right)^2 \approx 1 + 2\frac{R_0}{L}\left[\frac{R_0}{L} + \sqrt{1 + \left(\frac{R_0}{L}\right)^2}\right] > \left(\frac{l_{sym}}{L}\right)^2. \tag{61}$$

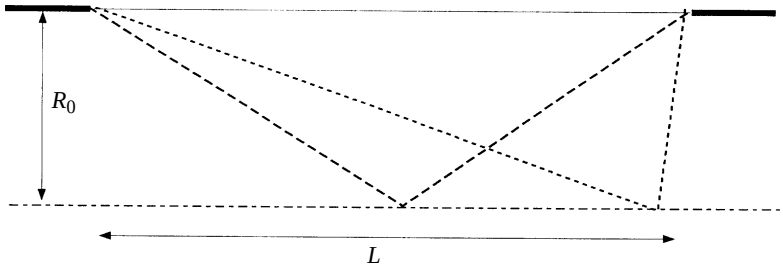

Figure 21. Sketch illustrating the axial extension of the tube wall during the buckling. The extension of the tube wall is minimized if the buckling is symmetric.

These rough estimates show that an axially symmetric buckling minimizes the extension of the tube wall. The effect is more pronounced for shorter tubes. Therefore, the maximum collapse of such tubes (e.g. $L/R_0 = 5$ as in case 1) is close to the centre of the tube. The longer the tubes, the more readily they collapse asymmetrically with the point of strongest collapse relatively closer to the downstream end. As was explained above, the buckling under constant pressure drop reduces the compressive load on the tube wall upstream of the point of strongest collapse. Therefore, the reduction in the compressive load after the buckling is more pronounced for longer tubes and the effect can be strong enough to change the character of the buckling instability.

Finally, we compare the exact geometrically nonlinear shell theory with Sanders' (1963) moderate rotation theory. Figure 22 compares the bifurcation diagram for the exact theory as shown in Figure 15 (solid lines) to the results obtained by using Sanders' approximation for the bending tensor (dashed lines). Sanders' theory gives accurate results for the prediction of the buckling point and for the initial post-buckling deformation. For larger deformations, Sanders' theory underestimates the tube stiffness significantly (on the stable branches, the deformation for a given load is overestimated, while on the unstable branches it is underestimated; the latter effect is due to the negative stiffness of the system on the unstable branches). The main features of the

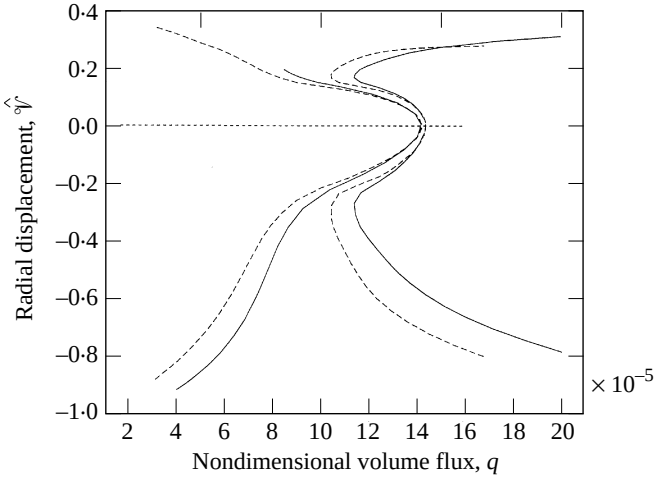

Figure 22. Bifurcation diagram for the tube with $L/R_0 = 10$, $p_{ext} = p_{entry} = 0$, $N_{buckl} = 2$. Equilibrium paths with and without fluid–solid coupling for the exact geometrically nonlinear theory (solid lines) and for Sanders' moderate rotation theory (dashed lines).

post-buckling behaviour (snap-through without fluid–solid coupling and immediate opposite-wall contact with fluid–solid coupling) are nevertheless captured.

The results presented in this study allow a critical review of previous work in which the tube deformation was modelled using ''tube laws''.

First, it should be noted that Figure 13 shows clearly, that a ''tube law'' in its simplest form (a functional relationship between transmural pressure and cross-sectional area of the tube, $p(z) - p_{ext} = \mathscr{P}[A(z)]$ cannot capture the essential details of the tube collapse. Since the tube is supported at the upstream and downstream ends, the corresponding cross-sectional areas have to be equal, whereas the pressure decreases continuously throughout its length. If the fluid flow were modelled using the full Navier-Stokes equations, we could expect some pressure recovery in the divergent part of the collapsed tube, but the fluid flow would still lead to an overall pressure drop between the upstream and downstream ends.

The tube law most commonly used is based on the post-buckling behaviour of rings or infinitely long tubes (Flaherty *et al.* 1972) and thereby neglects all axial forces and bending moments. Several authors [e.g. McClurken *et al.* (1981); Reyn (1987); Jensen & Pedley (1989)] have tried to improve the tube law by regarding it as a description of the tube elasticity in the transverse direction only. Based on the assumption that the cross-section of the collapsed tube is very flattened, they modelled the longitudinal elasticity of the tube by treating the tube wall as a pair of two-dimensional membranes whose spacing is proportional to the cross-sectional area. Hence, the tube law was modified to $p(z) - p_{\text{ext}} = \mathscr{P}[A(z)] - T\kappa$, where T and κ stand for the longitudinal tension and wall curvature, respectively. The wall curvature in the axial direction was assumed to be proportional to the second derivative of the cross-sectional area, i.e. $\kappa \sim A''$. With longitudinal tension, equal upstream and downstream cross-sectional areas are no longer equivalent to a vanishing pressure drop.

However, the wall deformation after the buckling, computed in this study, makes it questionable whether the assumptions leading to these modifications are justified. In the computations presented here, the tube cross-section never appeared very flattened. We observed either elliptical cross-sections of moderate aspect ratio or dumbbell-shaped cross-sections, in which the flow was already beginning to split up into two separate branches. In neither case was the configuration similar to the flow between two parallel membranes.

In cross-sections with opposite-wall contact, the assumptions leading to the above modifications are certainly not fulfilled: the flow in such cross-sections is split up into two separate branches, and the longitudinal wall curvature cannot be related to the second derivative of the cross-sectional area. The tube law in its original form (which includes the description of the wall contact) can be expected to give an accurate description of tube deformation if the tube is strongly collapsed over most of its length and if end effects can be neglected. However, no simple modification seems possible to improve the description of a partially collapsed tube.

It should be noted that Conrad (1969), in one of the earliest systematic collapsible tube experiments, comments on the very rapid collapse of the tube when buckling conditions are reached. His experimental procedure differs from the one envisaged in our study (he controlled the system by adjusting the flow resistance upstream of the collapsible tube) and he does not report when opposite-wall contact is observed for the first time. He mentions, however, that a minute change in the upstream resistance makes the tube buckle severely (transition between states ''13'' and ''14'' in figure 4 in his paper). The corresponding photographs of the tube indicate that immediate opposite wall contact is reached over about 25% of the tube's length after the buckling.

The findings presented in this study also have implications for the on-going controversy as to whether cylindrical shells conveying fluid lose their stability by flutter or by divergence [for a recent review see Païdoussis & Li (1993)]. In other words, should the large amplitude self-excited oscillations, observed in many collapsible tube experiments, be interpreted as flutter instabilities (i.e. limit cycle oscillations following a Hopf bifurcation) or as ''periodic divergence'', with the antinodes snapping through alternately between the positive and negative extremes of the modal form involved (Païdoussis & Li 1993; p. 186). The present study is implicitly based on the latter view, since only steady deformations were investigated. Obviously, our findings do not prove the ''periodic divergence'' scenario, but the severity of the collapse (snap-through or snap-through with immediate opposite-wall contact) indicates that the buckling process would be a highly dynamic process which could indeed initiate the oscillations observed. Further support for this view is given by Conrad's observation that ''during oscillation, the motion of the walls of the tube was essentially a succession, within a limited range, of the steady flow collapse states . . .'' (Conrad 1969; p. 291).

The results presented in this study were obtained for an ideal geometry without initial imperfections. However, it should be noted that the overall characteristics of the system are not affected by small imperfections. As mentioned above, the post-buckling deformations were computed by initially superimposing a small nonaxisymmetric pressure load on the fluid traction. This load-imperfection changed the tube behaviour in the vicinity of the buckling point, but the overall characteristics of the deformation were unaffected (see e.g. Figure 10: the ''imperfect'' tube still displays a marked snap-through).

The main weakness of the present study is the fluid model used. While lubrication theory is an improvement on previous one-dimensional models, the wall slopes at the downstream end of the collapsible segment are far too large to justify the small slope assumption. Nevertheless, the simple fluid model captures some interesting features of the flow, such as the division of the flow into two separate branches in a tube which collapses with $N_{\mathrm{buckl}} = 2$ circumferential waves and the concentration of the flow near the tube centreline for higher buckling wavenumbers. It is also interesting to note that Lowe & Pedley (1995) investigated the flow through a two-dimensional channel with a collapsible wall segment (modelled as an elastic membrane). They found surprisingly good agreement between lubrication theory and Stokes flow, even for strongly collapsed channels with large wall slopes. However, at physiologically realistic Reynolds numbers we would expect the flow to separate downstream of the narrowest cross-section. The pressure recovery in the divergent part of the collapsed tube would make the collapse less severe. We do not, however, expect the pressure recovery to be sufficient to change the post-buckling behaviour significantly.

To include all the relevant features into the model, we would have to solve the full Navier-Stokes equations. Furthermore, the solid solver needs to be extended to incorporate the contact problem. Work on both aspects is currently in progress.

5. CONCLUSIONS

We have studied the post-buckling behaviour of elastic tubes conveying a viscous flow using geometricllly nonlinear shell theory to model the tube wall and lubrication theory to model the fluid flow. It was found that without fluid–solid coupling, the tubes buckle with a snap through. The fluid–solid interaction accelerates the tube collapse to such an extent that the opposite walls come into contact immediately after buckling if the volume flux is kept constant during the buckling. However, if the pressure drop

through the tube is kept constant during the buckling, then the tube post-buckling deformation is slowed down by the fluid–solid coupling. We investigated the effects of variations in the upstream fluid pressure, in the axial pre-stretch and in the tube geometry. The exact geometrically nonlinear shell theory was compared to Sanders' (1963) moderate rotation theory and it was found that Sanders' theory only gives accurate results for the initial stages of the buckling. Finally, we discussed the implications of our results for collapsible tube models based on ''tube laws'' and the limitations and shortcomings of our model.

ACKNOWLEDGEMENTS

We wish to thank the Wellcome Trust for a studentship in Mathematical Biology (August 92–April 93) and the European Community ''Human Capital and Mobility Programme'' (Proposal: ERB4011GT920688) for their financial support. All computations were carried out on a Silicon Graphics Challenge XL computer, run by the University Computing Service, University of Leeds, and we would like to thank Dr J. Singh for his excellent user support. M. H. would also like to thank C. Dillan for many helpful discussions.

References

Becker, E. B., Carey, G. F. & Oden, J. T. 1984 *Finite Elements*: *An Introduction.* Englewood Cliffs, NJ: Prentice-Hall.

Bogner, F. K., Fox, R. L. & Schmit, L. A. 1967 A cylindrical shell discrete element. *AIAA Journal* **5,** 745–750.

Conrad, W. A. 1969 Pressure-flow relationships in collapsible tubes. *IEEE Transactions on Biomedical Engineering* **BME-16,** 284–295.

Crisfield, M. A. 1981 A fast incremental/iterative solution procedure that handles ''snap-through''. *Computers & Structures* **13,** 55–62.

Elad, D., Sahar, M., Avidor, J. M. & Einav, S. 1992 Steady flow through collapsible tubes: measurements of flow and geometry. *ASME Journal of Biomechanical Engineering* **114,** 84–91.

Esslinger, M. E. & Geier, B. M. 1971 On the buckling and postbuckling behaviour of thin-walled circular cylinders. In *RILEM International Symposium III.* Instituto Nacional de Technologia Industrial, Buenos Aires, Argentina.

Flaherty, J. E., Keller, J. B. & Rubinow, S. I. 1972 Post buckling behaviour of elastic tubes and rings with opposite sides in contact. *SIAM Journal of Applied Mathematics* **23,** 446–455.

Hart, V. G. & Shi, J. Y. 1992 Joined dissimilar elastic thin tubes containing steady viscous flow. *Journal of Mechanics and Physics of Solids* **40,** 1507–1527.

Heil, M. 1996 The stability of cylindrical shells conveying viscous flow. *Journal of Fluids and Structures* **10,** 173–196.

Heil, M. 1995 Large deformations of cylindrical shells conveying viscous flow. Ph.D. thesis. University of Leeds, Leeds, U.K.

Heil, M. & Pedley, T. J. 1995 Large axisymmetric deformations of a cylindrical shell conveying a viscous flow. *Journal of Fluids and Structures* **9,** 237–256.

Jensen, O. E. & Pedley, T. J. 1989 The existence of steady flow in a collapsed tube. *Journal of Fluid Mechanics* **206,** 339–374.

Kamm, R. D. & Pedley, T. J. 1989 Flow in collapsible tubes: a brief review. *ASME Journal of Biomechanical Engineering* **111,** 177–179.

Keller, H. E. 1977 Numerical solution of bifurcation and nonlinear eigenvalue problems. In *Applications of Bifurcation Theory* (ed. Rabinowitz, P.H.), pp. 359–384. New York: Academic Press.

Kirstein, A. F. & Wenk, E. 1956 Observations of snap-through action in thin cylindrical shells under external pressure. *Society for Experimental Stress Analysis Proceedings,* **XIV,** 205–214.

Kopal, Z. 1955 *Numerical Analysis.* London: Chapman & Hall.

LOWE, T. W. & PEDLEY, T. J. 1995 Computation of Stokes flow in a channel with a collapsible segment. *Journal of Fluids and Structures* **9,** 885–905.

MCCLURKEN, M. E., KECECIOGLU, I., KAMM, R. D. & SHAPIRO, A. H. 1981 Steady, supercritical flow in collapsible tubes. Part 2. Theoretical studies. *Journal of Fluid Mechanics* **109,** 391–415.

PAÏDOUSSIS, M. P. & LI, G. X. 1993 Pipes conveying fluid: a model dynamical problem. *Journal of Fluids and Structures* **7,** 137–204.

PEDLEY, T. J. 1980 *The Fluid Mechanics of Large Blood Vessels.* Cambridge: Cambridge University Press.

PRESS, W. H., TEUKOLSKY, S. A., VETTERLING, W. T., FLANNERY, B. P. 1992 *Numerical Recipes in FORTRAN,* 2nd edition. Cambridge: Cambridge University Press.

REYN, J. W. 1987 Multiple solutions and flow limitation for steady flow through a collapsible tube held open at the ends. *Journal of Fluid Mechanics* **174,** 467–493.

RIBREAU, C., NAILI, S. & LANGLET, A. 1994 Head losses in smooth pipes obtained from collapsible tubes. *Journal of Fluids and Structures* **8,** 183–200.

RIKS, E. 1979 An incremental approach to the solution of snapping and buckling problems. *International Journal of Solids and Structures* **15,** 529–551.

SANDERS, J. L. 1963 Nonlinear theories for thin shells. *Quarterly of Applied Mathematics* **21,** 21–36.

SCHNELL, W. & ESCHENAUER, H. 1984 *Elastizitätstheorie II*; *Schalen.* Mannheim: Bibliographisches Institut.

THIELEMANN, W. & ESSLINGER, M. 1967 Beul- and Nachbeulverhalten isotroper Zylinder under Aussendruck. *Der Stahlbau* **36,** 161–175.

WEMPNER, G. 1973 *Mechanics of Solids.* New York: McGraw-Hill.

WILD, R., PEDLEY, T. J. & RILEY, D. S. 1977 Viscous flow in collapsible tubes of slowly-varying elliptical cross-section. *Journal of Fluid Mechanics* **81,** 273–294.

YAMAKI, N. 1984 *Elastic Stability of Circular Cylindrical Shells.* Amsterdam: North-Holland.